Neuronal apoE4 induces early hyperexcitability in select populations of hippocampal neurons by altering Nell2 expression

Sung-Soo Jang[1,8], Dennis R. Tabuena[1,8], Brian Grone[1,2,8], Oscar Yip[1,3], Jessica Blumenfeld[1,4], Nicole Koutsodendris[1,5], Leonardo Ding[1], Qin Xu[1], Seo Yeon Yoon[1], Yadong Huang[1,2,3,4,5,6,7,*], Misha Zilberter[1,9,*]

[1] Gladstone Institute of Neurological Disease, Gladstone Institutes, San Francisco, CA, USA

[2] Gladstone Center for Translational Advancement, Gladstone Institutes, San Francisco, CA, USA

[3] Biomedical Sciences Program, University of California, San Francisco, CA, USA

[4] Neuroscience Program, University of California, San Francisco, CA, USA

[5] Developmental and Stem Cell Biology Program, University of California, San Francisco, CA, USA

[6] Department of Neurology, University of California, San Francisco, CA, USA

[7] Department of Pathology, University of California, San Francisco, CA, USA

[8] These authors contributed equally

[9] Lead contact

* Correspondence should be addressed to Misha Zilberter (misha.zilberter@gladstone.ucsf.edu) or Yadong Huang (yadong.huang@gladstone.ucsf.edu)

ABSTRACT

The impact of apolipoprotein E4 (apoE4), the strongest genetic risk factor for Alzheimer's disease (AD), on neuronal function remains unclear. We investigated this by examining excitatory neurons in the hippocampus of young and aged human apoE4 knock-in (apoE4-KI) and apoE3-KI mice using electrophysiology and single-nucleus RNA-sequencing (snRNA-seq). In young apoE4-KI mice, we identified region-specific subpopulations of excitatory neurons with hyperexcitability underlain by reduced cell size, which were eliminated by selective removal of neuronal apoE4. Aged apoE4-KI mice showed an increased fraction of hyperexcitable granule cells, a pronounced inhibitory deficit, and E/I imbalance in the dentate gyrus, contributing to network dysfunction. snRNA-seq analysis revealed neuron type-specific and age-dependent transcriptomic changes, identifying Nell2 overexpression in apoE4-KI mice. Reducing Nell2 expression in specific neuronal types of apoE4-KI mice with CRISPRi rescued their morphological and excitability phenotypes, supporting Nell2 overexpression as a cause for apoE4-induced neuronal dysfunction. Our findings highlight the early transcriptomic and morpho-electric alterations behind the apoE4-induced neuronal dysfunction in AD.

KEYWORDS:

Apolipoprotein E4 (apoE4); Alzheimer's disease (AD); Hippocampal excitability; Electrophysiology; Single-nucleus RNA-sequencing (snRNA-seq); Inhibitory dysfunction.

HIGHLIGHTS

- ApoE4 causes hyperexcitability of select hippocampal neurons in young apoE4 mice.
- ApoE4 causes dentate hyperexcitability and inhibitory deficit in aged apoE4 mice.
- snRNA-seq reveals apoE genotype-, cell type-, and age-dependent transcriptomic changes.
- Nell2 overexpression identified as a cause of apoE4-induced neuronal hyperexcitability.

INTRODUCTION

The ε4 allele of apolipoprotein E (apoE4) is the strongest genetic risk factor for Alzheimer's disease (AD) and lowers the age of onset of AD in a gene dose-dependent manner[1,2]. In most clinical studies, apoE4 carriers account for 60–75% of all AD cases[3], highlighting the importance of apoE4 in AD pathogenesis. Longitudinal studies in humans demonstrate that apoE4's detrimental effect on cognition is age-dependent and occurs before typical signs of AD arise[4], while structural imaging and cognitive studies have shown that healthy apoE4 carriers under the age of 40 exhibit reduced cortical thickness[5] as well as gray matter atrophy and worse cognitive performance[6]. All available data suggest that apoE4 plays a role in AD not just in its prodromal and active stages, but actually for decades before disease onset. Yet, there is still no clear understanding of how apoE4 expression promotes AD initiation and progression.

ApoE4 is also associated with hippocampal hyperactivity in non-demented young carriers and in mild cognitive impairment (MCI) and early AD patients[7,8]. The extent of apoE4-induced hippocampal hyperactivity predicts future memory decline[7], and targeting this pathology has been suggested as a strategy in treating AD-related cognitive dysfunction[9–12]. Additionally, apoE4 has been linked to subclinical epileptiform activity during stress[13]. It is also a known risk factor for acquired epilepsy (AE), with apoE4 carriers at higher risk for temporal lobe epilepsy (TLE)[8,13] and earlier TLE onset, especially post traumatic injury[14,15]. Moreover, apoE4 confers a six-fold higher probability of developing TLE treatment resistance[16] and is associated with diminished memory performance in TLE patients[17,18].

Notably, AE is a well-established early co-morbidity of AD[19], with studies reporting unprovoked seizures affecting between 10–22% and as high as 67% of AD patients[20]. Even such numbers are likely to be an underestimation of overall AD-related network hyperactivity as EEG studies reported subclinical epileptiform activity in up to 40% of AD patients[19,21–23]. Seizures occur in early AD stages and promote AD pathogenesis[24,25]. In addition, AE shares many symptoms and pathologies with AD[26,27], and drug-resistant TLE patients are at up to 10 times higher risk of developing AD[28]. However, the exact apoE4-positive proportion of those patients or the percentage of apoE4 carriers among AD patients diagnosed with AE is yet to be determined.

Besides its well-documented Aβ-dependent roles[29], apoE4 has less well-studied Aβ-independent functions in AD pathogenesis, as shown by *in vitro* and *in vivo* investigations[30,31]. Human apoE4 knock-in (apoE4-KI) mice lacking Aβ accumulation display sex- and age-dependent learning and memory deficits with age[32,33] and exhibit higher seizure incidence[34] and susceptibility[35] compared to apoE3-KI mice. Several potential mechanisms responsible for apoE4-related network hyperactivity and dysfunction have been reported, foremost among them inhibitory dysfunction[36] and interneuron death[31–33]. However, seizures begin to manifest in apoE4-KI mice at 5 months of age[34] prior to observable interneuron death[32,33] or inhibitory deficits[36], meaning that other mechanisms must be in play. It was shown that reducing early network hyperactivity by chronic pentobarbital treatment prevented

inhibitory neuron death and cognitive deficits months later[37], suggesting that inhibitory dysfunction at more advanced ages may be a direct consequence of preceding early network hyperactivity. Uncovering the causes of apoE4-driven early network pathophysiology will help advance our understanding of the role apoE4 plays in AD pathogenesis.

To investigate the age-dependent phenotypical differences in hippocampal excitatory neurons resulting from apoE4 expression and aging, we analyzed morpho-electric and intrinsic excitability parameters of excitatory neurons in hippocampal CA1, CA3, and dentate gyrus subregions of apoE-KI mouse brain slices collected at various ages using whole-cell patch clamp electrophysiology. To uncover any differences in network synaptic function and excitation/inhibition (E/I) balance, we also recorded spontaneous excitatory and inhibitory synaptic activity. We focused on two age groups: 7–9 months (young), when seizure symptoms begin to appear[34] but no cognitive dysfunction is detectable[33], and at 17–19 months (aged), when both pathophysiologies are present[32,33]. Female apoE3-KI and apoE4-KI mice were used as females have higher incidence of seizures[34] and cognitive dysfunction[33] in the context of apoE4 expression. To determine the cellular source of apoE4 responsible for observed phenotypes, we repeated our experiments in mice where the *apoE4* gene was selectively deleted in neurons (apoE4-fKI$^{Syn1\text{-}cre}$ mice) or astrocytes (apoE4-fKI$^{GFAP\text{-}cre}$ mice)[38].

ApoE4 expression modifies the transcriptomic profiles of brain cells[39–41] and our previous research has demonstrated that reversing these changes through chronic treatment with bumetanide normalizes network and cognitive impairments in apoE4-KI mice[39], indicating that normalizing gene expression alterations is an effective approach to prevent apoE4-associated pathologies. We performed single-nucleus RNA-sequencing (snRNA-seq) analysis of the hippocampus in three genotypes (apoE3-KI, apoE4-KI, and apoE4-fKI$^{Syn1\text{-}cre+}$) at four different ages (5, 10, 15, and 20 months) to identify the potential differentially expressed genes (DEGs) underlying the observed age- and cell type-dependent morpho-electric changes in neurons, and subsequently validated select genes' roles using targeted CRISPR interference (CRISPRi).

Our findings demonstrate that neuronal expression of apoE4 elicits early transcriptomic alterations and results in reduced cell size and associated neuronal hyperexcitability in pathological subpopulations of hippocampal excitatory neurons, along with region-specific progressive inhibitory deficit and E/I imbalance, all of which likely contribute to apoE4-induced pathophysiology in AD pathogenesis.

RESULTS

Neuronal intrinsic excitability (IE) is represented by a number of fundamental parameters recorded via the whole-cell patch clamp method. We restricted our main focus to passive neuronal properties modulating excitability such as cell membrane capacitance (C_m), which is proportional to the membrane surface area and reflects neuronal size[42], and input resistance (R_{in}). For active (stimulus-response) IE quantification, we focused on rheobase (minimal depolarizing current required for activation), spike latency (delay to first action potential in

response to a 1-s, 800pA ramped current injection), and firing gain (relationship between incremental 1-s depolarizing current step amplitude and the resulting spiking frequency). Together, these IE parameters represent the basics of the neurons' input-output function: how much input is required for their activation, how fast they activate, and how they convert input into spiking rate once activated. To examine the significant effects of age and apoE genotype on cell excitability, we compared a maximum likelihood model that included age and apoE genotypes with a null model that disregarded them. The resulting p-values for each of the excitability parameters were adjusted for multiple comparisons using the false discovery rate method (FDR=5%). For parameters exhibiting significant age or apoE genotype effects, we performed focused comparisons between apoE3-KI and apoE4-KI mice, or between two different ages within each apoE genotype, utilizing either a student's t-test or non-parametric tests, without applying any additional correction methods.

ApoE4 reduces the size of CA3 neurons and dentate granule cells in young mice

Both CA3 pyramidal cells (PCs) and dentate granule cells (DGCs) from young 7–9 months old apoE4-KI mice had smaller C_m values (Figures 1A and 1G) paralleled by higher input resistance (Figures 1B and 1H), suggesting reduced cell size in apoE4-KI mice. C_m and R_{in} values correlated significantly in apoE3-KI and apoE4-KI neurons (Figures 1M and 1Q), confirming that cell size modulates cell input resistance, as reported previously[43,44]. Interestingly, in aged (17–19-month-old) apoE3-KI mice, both cell types became smaller as evidenced by significantly lower C_m and higher R_{in} values compared to those in young apoE3-KI mice (Figures 1A, 1B, 1G, and 1H), abolishing the differences with age-matched apoE4-KI mice. Thus, apoE4's effects on the morpho-electric properties of CA3 PCs and DGCs starts early (at 7–9 months of age) and apoE3-expressing neurons catch up later with aging (at 17–19 months of age).

ApoE4 induces neuronal hyperexcitability in young mice

In young apoE4-KI mice (7–9 months of age), both CA3 PCs and DGCs exhibited a pronounced hyperexcitability phenotype compared to neurons from young apoE3-KI mice. CA3 PCs had higher firing gain (Figure 1D) as well as lower rheobase values (Figure 1E), while age and apoE genotype-mediated differences in spike latency were not statistically significant (Figure 1F). DGCs showed no apoE-dependent firing gain phenotype (Figures 1I and 1J), but did exhibit lower rheobase (Figure 1K) and spike latency (Figure 1L) in apoE4-KI mice as compared to those from apoE3-KI mice. Consistent with their reduced C_m and increased R_{in} values, CA3 PCs and DGCs from apoE3-KI mice at 17–19 months of age, compared to younger apoE3-KI mice, showed significantly increased excitability (Figures 1C–1F, 1L, and S2B), eliminating the differences with neurons from aged apoE4-KI mice.

The apparent similarity between cell type- and age-dependent neuronal size (C_m) and IE phenotypes suggests that these neuronal properties might be related as shown previously in other AD models[45,46]. To uncover this relationship, we explored the correlations between C_m and IE parameters in neurons from young apoE-KI mice. In both CA3 PCs and DGCs, every IE parameter which reflected a hyperexcitable phenotype in apoE4-KI mice

correlated significantly with C_m values, while the corresponding parameter in both cell types from apoE3-KI mice showed no such correlation (Figures 1N–1P and 1R–1T), indicating that apoE4-induced hyperexcitability is indeed at least in part underlain by reduced cell size.

In contrast, we found no significant IE phenotype in CA1 PCs of apoE4-KI mice versus those of apoE3-KI mice at any age (Figures S1C–S1F), indicating neuronal cell type specificity of apoE4 effect. Although CA1 PCs from apoE4-KI mice did exhibit smaller C_m values in both age groups compared to those from apoE3-KI mice (Figures S1A and S1B), the difference was less pronounced (C_m in 7–9-month-old apoE4-KI mice: CA1 PCs 87%, CA3 PCs 82%, DGCs 82% vs. 7–9-month-old apoE3-KI mice; Table S1) and did not translate to significant differences in R_{in} (Figure S1B). We also found no aging-related changes in C_m or R_{in} values, nor in excitability parameters of CA1 PCs across apoE genotypes (Figure S1A–S1F).

ApoE4 increases population of immature-like dentate granule cells with aging

We also recorded a distinct sub-population of DGCs with immature electrophysiological properties, referred to as Type I DGCs[47] in both apoE3-KI and apoE4-KI mice. Type I DGCs were characterized by their inability to sustain firing under higher stimulation intensities (Figures 2A and 2B) and displayed a smaller cell size and hyperexcitability phenotype, as indicated by lower C_m values (Figures 2D and 2I), higher input resistance (Figures 2E and 2J), higher firing gain (Figures 2F and 2K), lower rheobase (Figures 2G and 2L), and lower spike latency (Figures 2H and 2M) compared to more mature Type II DGCs[47]. While the relative population of Type I DGCs did not differ between young apoE3-KI and apoE4-KI mice (33% in apoE3-KI mice vs. 35% in apoE4-KI mice at 7–9 months of age) (Figure 2C), aged apoE4-KI mice possessed a significantly higher proportion of Type I DGCs (43% in apoE3-KI mice vs. 64% in apoE4-KI mice at 17–19 months of age; $p = 0.0008$, Cochran-Mantel-Haenszel test) (Figure 2C). As Type I DGCs are hyperexcitable compared to Type II DGCs, their increased fraction resulted in a persistent dentate hyperexcitability phenotype in aged apoE4-KI mice (Figures 2O and 2Q), despite no apoE isoform-dependent IE differences within each DGC subtype at the same old age (Figures 1J-L and 2K-M).

Finally, we compared other IE-related parameters such as the resting membrane potential (RMP), maximal firing rate, and spike accommodation (Figure S2), and action potential (AP) waveform parameters (Figure S3). Significant differences were only observed in CA3 PCs from young apoE4-KI mice, seen as elevated maximal firing rate (Figure S2B) and increased fast afterhyperpolarization (fAHP) amplitude (Figure S3E) compared to those from young apoE3-KI animals.

Taken together, young apoE4-KI mice exhibited a cell type-specific hyperexcitability phenotype in CA3 PCs and DGCs which was associated with reduced cell size. Aging did not affect this phenotype in apoE4-KI mice, but did result in a significantly increased population of immature-like and hyperexcitable Type I DGCs, promoting dentate hyperexcitability. In contrast, aging resulted in smaller and more excitable CA3 PCs and DGCs in apoE3-

KI mice, highlighting the intricate relationship between apoE isoforms, age, cell size, and intrinsic excitability in hippocampal neurons.

Removal of apoE4 from neurons rescues their size and hyperexcitability phenotypes.

ApoE is largely made in astrocytes in brains, although it can also be produced in stressed neurons[40,41,48]. To find out whether apoE4-related morpho-electric and excitability phenotypes were caused by neuronal or astrocytic apoE4 expression[38,49], we performed similar experiments in 7–9-month-old apoE4-KI mice in which the *APOE4* gene was selectively deleted in either neurons (apoE4-fKI$^{Syn1\text{-}Cre}$ mice[34]) or astrocytes (apoE4-fKI$^{GFAP\text{-}Cre}$ mice[38]). By recording passive and active properties of CA3 PCs from these mice, we observed that neuronal apoE4 removal resulted in full normalization of all altered parameters — C_m and R_{in}, firing gain, rheobase, and spike latency — to the levels seen in apoE3-KI mice (Figures 3A–3H), indicating the critical role of neuronal apoE4 in apoE4-induced morpho-electronic and excitability changes. Deletion of apoE4 in neurons also abolished all correlations between C_m and primary IE parameters (Figures 3G–3I). In sharp contrast, removal of astrocytic apoE4 had no significant effect on either the neuronal cell size (Figure 4A) or excitability (Figures 4C–4F), supporting the critical role of neuronal apoE4 in apoE4-induced morpho-electronic and excitability changes.

ApoE4-induced morpho-electric phenotype is heterogenous with distinct subpopulations of small and hyperexcitable neurons.

To further explore the correlations between CA3 excitability parameters and identify hyperexcitable neurons using a data-driven approach, we employed the k-means method to cluster neurons based on their morpho-electric properties. We pooled CA3 PCs from all genotypes and ages, normalizing values prior to clustering (Figure 5A). We then used k-means clustering to identify two clusters ($k = 2$), with each cluster described by its *centroid*, the set of mean parameter values (Figure 5B). Clusters naturally divided primarily along morpho-electric and excitability parameters that were significantly different between young apoE3 and apoE4-expressing CA3 PCs, and not along parameters that did not show differences across apoE genotypes and ages (Figures S2 and S3), indicating that clustering analysis is capturing key differences between pathologically hyperexcitable and healthy or normal neurons.

To validate the results and ensure the robustness of the centroid characteristics, we utilized an 80:20 hold-out cross-validation approach where we randomly selected 80% of the neurons to use for cluster fitting, with the remaining 20% of the neurons classified based on the resulting clusters (Figure 5C). This was repeated for 1000 iterations and the cluster centroids along with neuronal cluster assignment were recorded for each iteration. The centroids remained stable across iterations, emphasizing the significance of the identified parameters (Figure 5B). The probability of a cell maintaining its membership in the original cluster (Figure 5C, lower panel) and the probability of each iteration to match the clustering of the original clustering were consistently well above chance (50% when $k = 2$; Figure 5C, right panel), indicating that the overall cluster separation is not subject to outliers

or chance, and that the identified morpho-electric parameters are indeed key variables in cell classification. In contrast, validation with three clusters (*k* = *3*) demonstrated high variability and unreliability (Figure 5D), indicating the presence of only two primary clusters.

To assess the overlap between hyperexcitable cells in apoE3-KI mice and normal cells in apoE4-KI mice, we examined the distance of each neuron from the cluster centroids (Figure 5E), which reflects the similarity (small distance) or dissimilarity (large distance) of each cell to the cluster centroid. By plotting the cells' distances on a scatter plot, the k-means classification could be visualized, with decision (unity) line representing equidistance from each centroid (Figure 5F). Each neuron's signed distance to the unity line (its residual value; Figure 5F, right panel) is therefore representative of its strength of cluster membership. Analysis of membership strength revealed the impact of neuronal apoE4 expression and age on cell classification, showing significantly more hyperexcitable neurons in young apoE4-KI mice compared to age-matched apoE3-KI mice, with more apoE3-KI neurons shifting into the hyperexcitable cluster with age (Figure 5G). However, a proportion of apoE4-KI neurons did exhibit strong membership in the normal cluster at both ages, indicating selective vulnerability of CA3 PCs to apoE4 effects. Finally, selective deletion of neuronal apoE4 in young apoE4-fKI$^{Syn1\text{-}Cre+}$ mice resulted in a significant depletion of the hyperexcitable CA3 PC cluster compared to their Cre-negative^{-} littermates which resembled apoE4-KI mouse cluster distribution (Figure 5G).

The same analysis was performed for DGCs and CA1 PCs. Type II DGCs displayed similar patterns of hyperexcitability classification, primarily determined by differences in morpho-electric parameters R_{in} and C_m (Figure S4A). Significantly more type II DGCs in young apoE4-KI mice belonged to the hyperexcitable cluster compared to young apoE3-KI type II DGCs (Figure 5H), while no age- or apoE genotype-dependent differences were observed in type I DGCs (Figure 5I), likely due to lower variability in cell size/excitability and less reliable clustering indicating homogeneity among type I DGCs (Figures S4B, S4E). Cluster analysis combining both type I and II DGCs robustly identified both hyperexcitable and normal clusters, with membership primarily dependent on DGC type rather than age or apoE genotype (Figures S4M-S4N). Meanwhile, in CA1 PCs, no significant apoE genotype- or age-related differences in hyperexcitable populations were observed (Figure 5J), despite the presence of a robust clustering of hyperexcitable and normal cells (Figure S4C, S4F)

Comparing the centroids of all cell types highlighted consistent divisions, with hyperexcitable cells defined by morpho-electric parameters (R_{in} and C_m) and IE parameters (firing gain, rheobase, and spike latency), but not by AP waveform or other membrane properties (Figure 5K). Cluster enrichment was ultimately determined by cell type-, apoE genotype-, and age-mediated differences in these parameters, reinforcing our conclusion that neuronal apoE4 expression in select sub-populations of neurons results in reduced cell size and consequent intrinsic hyperexcitability.

Region-specific and age-dependent synaptic excitation-inhibition imbalance in the hippocampus of apoE4-KI mice.

Another major mechanism contributing to hyperactivity and cognitive deficits in apoE4-KI mice is synaptic dysfunction, especially the loss of inhibitory function reported previously[32,36]. To investigate the network and synaptic consequences of apoE4 expression, we recorded spontaneous excitatory post-synaptic currents (sEPSCs) and inhibitory post-synaptic currents (sIPSCs) in CA3 PCs and DGCs in both age groups. CA3 PCs in apoE4-KI mice displayed higher sEPSC frequency and similar sEPSC amplitude compared to those in apoE3-KI mice at 7–9 months of age (Figures 6A and 6B, and Figure S5A), consistent with hyperexcitability of these cells given the recurrent excitation in CA3 local networks[50]. We found no apoE genotype-specific or age-dependent differences in sIPSC frequency or amplitude in CA3 PCs between apoE4-KI and apoE3-KI mice at 7–9 months of age, indicating unaltered inhibitory tone across the apoE genotypes at this young age (Figure 6C; Figures S5C and S5D). Increased excitatory drive together with unchanged inhibitory input resulted in a higher excitatory-to-inhibitory (E-I) ratio in CA3 PCs in apoE4-KI mice at 7–9 months of age (Figure 6E). By 17–19 months of age, both the excitatory input frequency and E-I ratio significantly increased in CA3 PCs in apoE3-KI mice, abolishing the differences with CA3 PCs in apoE4-KI mice, mirroring the age-related trend observed in excitability of these cells. We found no differences in sEPSCs in DGCs from apoE4-KI mice at either age (Figures 6F and 6G; Figures S5E and S5F). At the same time, in line with our previous reports on accelerating hilar interneuron death in apoE4-KI mice[32,33], DGCs displayed a progressive reduction in sIPSC frequency with age (Figures 6H and S5G), resulting in significantly higher E-I ratios in apoE4-KI mice at 17–19 months of age (Figure 6J).

Neuronal cell type-specific and age-dependent transcriptomic changes caused by neuronal apoE4 expression.

The apparent heterogeneity of apoE4 effect in neuronal populations appears similar to the cell selectivity of apoE4 effect on neuronal transcriptomes that we reported recently[40] and suggests a potential transcriptomic signature behind susceptibility and resilience of apoE4-expressing neurons. To uncover any apoE4-related gene expression differences in different types of hippocampal neurons, we analyzed our previously published snRNA-seq datasets obtained from apoE3-KI and apoE4-KI mouse hippocampi at different ages (Figures 7A and 7B)[40]. To select differentially expressed genes (DEGs) whose transcriptional profile changes fit the observed neuronal morpho-electric phenotypes in an apoE genotype-, cell type-, and age-dependent manner, we focused on clusters 1 and 2 (DGCs) as well as 6 (CA2/3 PCs) and applied the following criteria (Figure 7C): genes differentially expressed in (a) apoE4-KI mice versus apoE3-KI mice at 5 months and (b) at 10 months, (c) in cells with high apoE expression from 10-month-old apoE4-KI mice (we classified cells as apoE-expression-high if they express apoE mRNA at >2 SD above the median expression for that cell type), (c) not in neurons from 10-month-old fE4KI$^{Syn1\text{-}Cre+}$ mice versus those from 10-month-old apoE4-KI mice, (d) not in neurons from 20 month-old apoE4-KI mice versus those from 20-month-old apoE3-KI mice; and (e) in neurons from 20-month-old apoE3-KI

mice versus those from 5-month-old apoE3-KI mice, with same directional change as in (a–c). This last criterion was important to include since we observed a significant reduction in cell size together with increased excitability of both CA3 PCs and DGCs in aged vs. young apoE3-KI mice (Figure 1). From the initial pool of 552 DEGs for DG1 (Table S5), 889 for DG2 (Table S6), and 492 for CA2/3 PCs (Table S7) clusters in 5 month-old mice (Figure 7C), our analysis pipeline yielded 2 final candidate DEGs for cluster DG1 (Figure 7D), 13 for cluster DG2 (Figure 7E) and 7 for CA2/3 PC cluster (Figure 7F).

Targeted reversal of Nell2 expression in neurons from young apoE4-KI mice rescues their size and hyperexcitability phenotypes.

Following the identification of a number of DEGs that may modulate the pathological impact of apoE4 on neuronal excitability and/or susceptibility or resistance to apoE4 effects, we employed the KRAB-mediated CRISPRi gene regulation technique[51] in young apoE4-KI mice to validate their functional significance by altering the expression of selected DEGs toward their expression levels in apoE3-KI mice. We selected two candidate genes based on our snRNA-seq results in Figures 7D and 7E: Nell2 (neural epidermal growth factor-like protein 2), the only DEG shared between CA2/3 PC and DGC2 clusters, and Mdga2 (MAM domain containing glycosylphosphatidylinositol anchor 2), the only DEG shared between DGC1 and DGC2 clusters. We designed custom recombinant lentiviruses targeting each selected DEG for CRISPRi as well as dCAS9 vector lentivirus that would also induce mCherry expression for fluorescence tagging of target neurons, and injected them into the DG/CA3 hippocampal region in 5-month-old female apoE4-KI mice. Two months later, we recorded CA3 PC and DGC electrophysiological parameters in hippocampal slices from the injected mice. Using mCherry fluorescence as a guide, we could target both transduced CRISPR-positive and control CRISPR-negative neurons in the same slice for patch-clamp recordings (Figure 8A).

Nell2 is a kinase C-binding[52,53] glycoprotein that has been shown to have multiple roles in regulating neuronal proliferation, survival, differentiation, polarization, as well as axon guidance and synaptic functions[54–56]. mCherry+ Nell2-CRISPRi-transduced CA3 PCs and DGCs (Figure 8A) had increased cell size (Figures 8B and 8K), as determined by increased C_m values, and displayed significantly higher rheobase and spike latency values (Figures 8F, 8G, 8O, and 8P) compared to neighboring mCherry- non-transduced neurons, indicating reduced excitability of the Nell2-CRISPRi-transduced neurons. mCherry+ CA3 PCs also showed decreased firing gain (Figures 8D and 8E), indicating a rescue of that cell type-specific phenotype, although we observed no differences in firing gain between mCherry+ and mCherry- DGCs (Figures 8M and 8N), consistent with the lack of firing gain phenotype in those neurons (Figures 2C and 2D). Importantly, changes in C_m correlated significantly with changes in each of the three phenotypic IE parameters (Figures 8H–8J, 8R, and 8S), supporting our hypothesis that apoE4-related neuronal size and excitability phenotypes are related.

Mdga2 is a gene previously implicated in ASD-related epilepsy[57]. We found no difference in any excitability parameters or size in mCherry+ Mdga2-CRISPRi-transduced neurons versus mCherry- neurons (Figures S6H–S6M). Although this data disproves the involvement of Mdga2 in apoE4-induced neuronal morpho-electric phenotype, it does confirm that the CRISPRi procedure itself does not affect neuronal parameters and therefore can serve as a "negative" CRISPRi control. Altogether, our CRISPRi validation study confirmed the critical role of Nell2 overexpression in mediating early apoE4-induced neuronal morpho-electric deficits. This substantiates the targeted reversal of apoE4-induced transcriptomic changes as a promising strategy for early therapeutic intervention in apoE4-related AD.

DISCUSSION

Multiple studies have consistently demonstrated increased task-related activation of the hippocampus in young individuals who carry the *apoE4* allele[7,58,59]. Notably, the degree of apoE4-induced hippocampal hyperactivity has been shown to predict future memory decline[7]. Female apoE4-KI mice develop seizures from the age of 7 months[34], indicating that apoE4-induced pathological changes in network excitability occur prior to the manifestation of observable cognitive deficits[33]. While genetic mouse models of AD that overexpress APP and accumulate beta-amyloid (Aβ) develop network hyperactivity and seizures at ages preceding plaque formation[60–63], the apoE4-KI mice used in our study develop network deficits and hyperactivity[31] in the absence of Aβ accumulation, suggesting an apoE4-specific and Aβ-independent effect. Our findings indicate that network pathophysiology in apoE4-KI mice is attributable to the neuronal expression of apoE4, which modifies the transcriptome and results in early neuron subtype-specific atrophy and intrinsic hyperexcitability of hippocampal excitatory neurons, ultimately leading to region-specific and age-dependent dysfunction in the E-I balance in aged apoE-KI mice.

In APP-overexpressing AD mice, network hyperactivity is underlain by excitatory neurons' hyperexcitability[60,61,64] as well as by inhibitory deficit[36,65] resulting from Aβ toxicity. Multiple intrinsic excitability parameters mediating the Aβ effect on neuronal hyperexcitability have been reported in a number of transgenic amyloidosis mouse models, including depolarized neuronal resting membrane potential[60,61], depolarized reversal potential of GABA-mediated inhibitory synaptic currents[61], increased firing gain[66,67], reduced spike latency[67], as well as altered AP width[45,67] and amplitude[45]. We found that CA3 PCs and DGCs in young apoE4-KI mice are hyperexcitable in their subthreshold (rheobase, spike latency) and suprathreshold (firing gain, max firing rate, accommodation) parameters. The observed apoE4-driven hyperexcitability phenotype resembles those reported in mouse amyloidosis models in some parameters, but differs in others: for example, we found no changes in resting membrane potential or AP shape.

Neuronal excitability is also mediated by passive neuronal properties, such as R_{in} and C_m. Since specific membrane capacitance in neurons is remarkably constant at $0.9\mu F/cm^2$ across all cell types[68], C_m is a direct

representation of total membrane surface area and therefore, cell size[42]. In our study, CA3 PCS and DGCs in young apoE4-KI mouse hippocampus were consistently smaller than those in age-matched apoE3-KI mouse hippocampus, as evidenced by lower C_m values. The patch-clamp measurement of C_m is most sensitive to the proximal regions so the observed reduced neuronal size is likely to include the soma and proximal dendritic morphology, although we cannot exclude differences in more distal dendritic regions as reported by us previously[49]. Our results are consistent with previous reports: apoE4 correlated with smaller neuron size in resected tissue from human epilepsy patients[69]. Neuronal apoE4 expression in mice results in reduced dendritic morphology[49] and has been shown to exert a disruptive effect on dendritic integrity in response to excitotoxic injury[70]. Reduced C_m has also been reported in human induced pluripotent stem cell (iPSC)-derived neurons from AD patients[45] as well as in neurons from APP/PS1 mouse AD model[46]. In CA3 PCs and DGCs from young apoE4-KI mice, every IE parameter that differed from those in apoE3-KI mice correlated significantly with C_m, while no such correlation was observed in those neurons in apoE3-KI mice, suggesting that reduced cell size at least in part underlies apoE4-induced neuronal hyperexcitability. Previous studies on different AD mouse models reported similar relationship: decreased neuronal size was shown to underlie hyperexcitability and hyperactivity of CA1 PCs in APP/PS1 mouse model of AD[46]; analogous causality has been reported in human iPSC-derived neurons carrying PS1 and APP mutations[45].

In the brain, apoE is primarily expressed by astrocytes, but in response to stress or injury neurons also begin to express apoE[30,71,72]. Neuronal, but not astrocytic, apoE4 undergoes proteolytic cleavage, generating toxic apoE4 fragments that have been shown to cause multiple pathologies including tau hyperphosphorylation, mitochondrial impairment, and neurodegeneration[72–74]. Neuronal apoE4 expression is also responsible for the impairment and death of hilar somatostatin-expressing interneurons, which correlated with learning and cognitive deficits in aged apoE4-KI mice[32,33,38]. However, the exact functional consequences of apoE4 expression in hippocampal excitatory neurons have not been demonstrated until now. Here we show that apoE4 detrimental effects on neuronal size and excitability are specific to its expression in neurons: removal of apoE4 in neurons of young apoE4-fKI$^{Syn1\text{-}cre}$ mice normalized CA3 PC excitability as well as neuronal size and input resistance to apoE3-KI levels, while astrocytic apoE4 removal in apoE4-fKI$^{GFAP\text{-}cre}$ mice showed no such rescue.

Our clustering analysis revealed that not all cells, even within a given type, are equally vulnerable to apoE4's detrimental effect on neuronal size and excitability. We uncovered two distinct subpopulations of neurons within each cell type: healthier, "normal" neurons as well as small and hyperexcitable ones, with the enrichment of each subpopulation dependent on cell type, apoE genotype, and age. This is consistent with our recent study[40] showing that a subpopulation of neurons upregulates their apoE4 expression, contributing to selective cellular vulnerability to AD-related neurodegeneration. The same study showed that neuronal apoE expression levels are also age-dependent, with high apoE4-expressing neuron population peaking at 10 months of age, while high apoE3-expressing neurons reached maximum at 15 months of age. This is comparable with what we observed in the current study, with many CA3 PCS and DGCs shifting into the hyperexcitable subpopulation in apoE4-KI

mice at 7–9 months of age and in apoE3-KI mice at 17–19 months of age, suggesting that heterogenous apoE4 expression in neurons might drive electrophysiological heterogeneity during aging, which warrants further in-depth studies in the future.

CA3 PCs and Type II DGCs in aged apoE3-KI mice "catch up" with those from apoE4-KI mice, becoming smaller and more excitable, presumably as the result of normal aging[75–77], thus abolishing the early morpho-electric difference between apoE4-KI and apoE3-KI mice at old ages. The fact that aged apoE3-KI mice do not develop epilepsy even though their excitatory cells become more excitable suggests that additional mechanisms are involved in promoting the apoE4-induced network dysfunction at more advanced ages. We found that the population of smaller and hyperexcitable immature-like Type I DGCs was significantly more enriched in aged apoE4-KI mice, likely contributing to the maintained overall DGC hyperexcitability phenotype compared to apoE3-KI animals. We also found a progressive inhibitory deficit specifically in the dentate gyrus of apoE4-KI mice, manifested as decreased spontaneous inhibitory input frequency resulting in a significantly higher excitation-inhibition (E-I) ratio at 17–19 months, a pathology further promoting network and behavioral dysfunction in apoE4-KI mice at this advanced age[32,33,78,79]. Preceding hippocampal network hyperactivity at 7–9 months may actually be the primary driver of the inhibitory dysfunction in aged apoE4-KI mice: we have previously shown that reducing network hyperactivity at 9 months by chronic 6-week treatment with pentobarbital, a $GABA_A$ receptor potentiator, prevented hilar interneuron death and cognitive impairment in apoE4-KI mice 7 months later[37].

The exact mechanism behind the apoE4-induced neuronal atrophy and associated hyperexcitability remains unclear. However, despite the radically different pathological triggers, our observations of similar neuronal atrophy and hyperexcitability in apoE4-KI mice lacking Aβ accumulation, to those reported in mouse amyloidosis models, imply a shared pathway of action. One such pathway may involve tau[80,81]: neuronal apoE4 can induce an increase in tau phosphorylation[82] and neurodegeneration[49], mirroring the Aβ effects on tau reported in other studies[83–86]. Moreover, removal of endogenous tau prevented neuronal loss and cognitive deficits in both apoE4-KI mice[32] and APP transgenic mice[87,88]. In our most recent study, we reported that removal of neuronal apoE4 is protective against tau pathology, network hyperexcitability, neurodegeneration, and neuroinflammation in a tauopathy mouse model[41].

Our previous study highlighted the potential therapeutic benefits of reversing apoE4-induced transcriptomic changes on ameliorating network and cognitive deficits[39]. Now, our snRNA-seq analysis revealed a number of genes that exhibited differential expression patterns which mirrored the observed apoE4-specific and aging-dependent electrophysiological changes; these DEGs may influence neuronal morphology and excitability directly, or alternatively regulate the susceptibility or resilience to neuronal apoE4 toxicity. Importantly, we identified a specific upregulation of Nell2 in CA3 PCs and DGCs of young apoE4-KI mice, which was abolished

upon neuronal removal of apoE4. CRISPR$_i$ validation provided proof for the critical role of Nell2 overexpression in mediating apoE4-induced early neuronal morpho-electric deficits, as reducing Nell2 expression rescued neuronal size and hyperexcitability phenotype in both CA3 PCs and DGCs of young apoE4-KI mice.

Nell2 is a glycoprotein that is specific to glutamatergic neurons in pyramidal and granule cell layers in CA1-3 and dentate gyrus, respectively[56]. It has been shown to interact with protein kinase C through its EGF-like domain[52] and to modulate MAPK activity[54]. Furthermore, Nell2 shares domains with thrombospondin-1, a protein involved in regulating cell proliferation and apoptosis[89]. It is secreted as a trophic factor[54,55], however its alternative splicing variant is cytoplasmic and was shown to be involved in intracellular signaling[90] (such as binding to PKCβ1[52]) instead. Increased Nell2 protein expression was observed in hippocampus of 5XFAD AD model mice[91]. In addition, NELL2 and MDGA2 circular RNA (circRNA) expression was found to be upregulated in cortical tissue of AD patients[92]. Clearly, the roles of Nell2 in neuronal morphology and/or excitability, especially in the context of apoE4, warrants further in-depth studies in the future.

In summary, our study provides evidence that the expression of apoE4 in hippocampal excitatory neurons of young apoE4-KI mice induces significant transcriptomic alterations, including overexpression of Nell2 in CA3 PCs and DGCs, leading to atrophy and hyperexcitability in specific neuronal subpopulations. These findings suggest a causative timeline of apoE4-induced network dysfunction with aging: during early stages, neuronal apoE4 expression triggers cell type-specific transcriptomic alterations, neuronal atrophy, and hyperexcitability, culminating in network hyperactivity. As the apoE4-KI mice age, this process further contributes to the loss of hilar interneurons and inhibitory deficits, accompanied by a pathological increase in hyperexcitable immature-like Type I DGCs. Consequently, hippocampal network dysfunction and cognitive impairment develop, whereas aged apoE3-KI mice display resistance due to maintained inhibitory function despite increased excitability of excitatory neurons. To develop effective intervention strategies for apoE4-related AD, further investigations are warranted to unravel the precise mechanisms underlying apoE4-induced detrimental changes in excitatory neurons and the dysfunction of inhibitory neurons in the hippocampus. By deepening our understanding of these underlying processes, we can pave the way for potential therapeutic interventions specifically targeting apoE4-related AD.

Acknowledgments: We thank Huang lab staff for their valuable discussions about the experimental design as well as data analyses and interpretation. We thank Reuben Thomas for his advice on statistical analysis methods. We also thank Eric Chow and the staff at the UCSF Center for Advanced Technology Core for advice and support with RNA sequencing and Theodora Pak for editorial assistance.

Author Contributions

SSJ, DT and MZ carried out the study and analyzed the data. BG, LD, and MZ performed snRNA-seq data analysis. QX helped design CRISPRi vectors. OY, JB, and NK participated in some experiments. SYY managed mouse lines. MZ and YH designed and supervised the study. MZ, DT, and YH wrote the manuscript.

Funding

This study was supported by the National Institute on Aging grant R01AG061150 to MZ, R01AG055682, R01AG071697, and P01AG073082 to YH.

Declaration of interests

YH is a cofounder and scientific advisory board member of GABAeron, Inc. Other authors declare no competing interests.

FIGURES

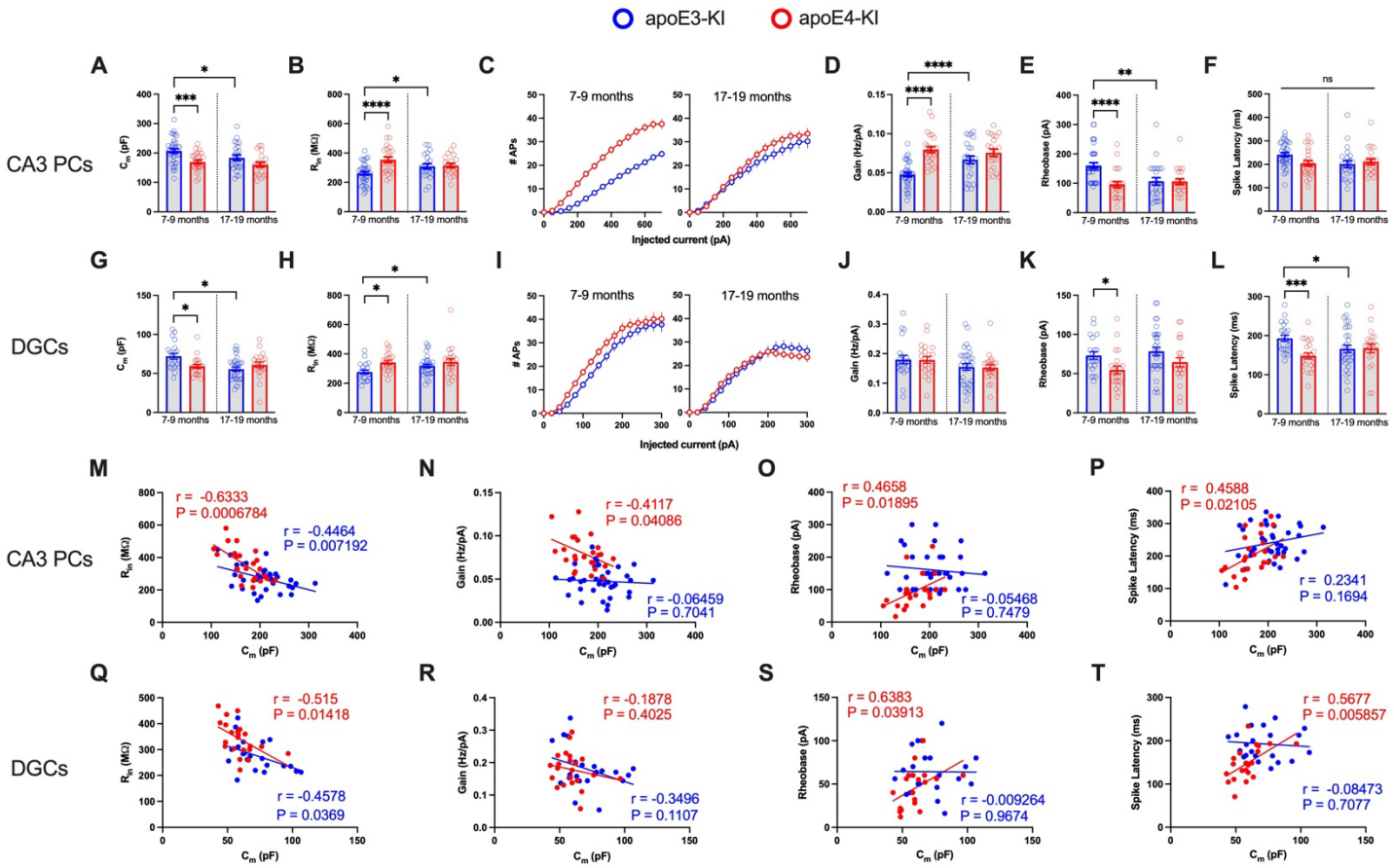

Figure 1. ApoE4-driven intrinsic electrophysiological differences in hippocampal excitatory neurons.

(A) Cell membrane capacitance (C_m) values for CA3 pyramidal cells (PCs) from apoE3-KI (blue) and apoE4-KI (red) mice at ages of 7–9 months and 17–19 months.

(B) Input resistance (R_{in}) for CA3 PCs from apoE3-KI and apoE4-KI mice.

(C) CA3 PCs input current – firing rate relationship (I-F Curve), the average number of spikes elicited by 1sec epochs of incremental depolarizing current injection.

(D) CA3 PC firing gain values, quantified as the linear slope of the I-F curve.

(E) CA3 PC rheobase values, representing the minimum 1s depolarizing current required to elicit an action potential.

(F) CA3 PC spike latency values, representing the delay to first spike in response to a 800pA, 1sec ramped depolarizing current injection.

(G) C_m values for dentate granule cells (DGCs).

(H) DGC R_{in} values.

(I) Average DGC I-F Curves.

(J) DGC firing gain values.

(K) DGC rheobase values.

(L) DGC spike latency values.

(M) Correlation between C_m and R_{in} values in 7–9 month-old apoE3-KI (blue) and apoE4-KI(red) CA3 PCs. Numbers represent Pearson's correlation coefficient and corresponding p-values.

(N) Correlation between C_m and firing gain values in 7–9 month-old CA3 PCs.

(O) Correlation between C_m and rheobase values in 7–9 month-old CA3 PCs.

(P) Correlation between C_m and spike latency values in 7–9 month-old CA3 PCs.

(Q) Correlation between C_m and R_{in} values in 7–9 month-old DGCs.

(N) Correlation between C_m and firing gain values in 7–9 month-old DGCs

(O) Correlation between C_m and rheobase values in 7–9 month-old DGCs.

(P) Correlation between C_m and spike latency values in 7–9 month-old DGCs.

*p<0.05, **p<0.01, ***p<0.001, ****p<0.0001, unpaired two-tailed t-test or Mann-Whitney U test. N= 8 and 7 mice for CA3 PCs from 7–9 month-old apoE3-KI and apoE4-KI mice, respectively; N= 4 and 3 for DGCs from 7–9 month-old apoE3-KI and apoE4-KI mice. N= 6 and 4 mice for CA3 PCs from 17–19 month-old apoE3-KI and apoE4-KI mice; N= 5 each for DGCs from 17–19 month-old apoE3-KI and apoE4-KI mice. See also Supplementary Table 1.

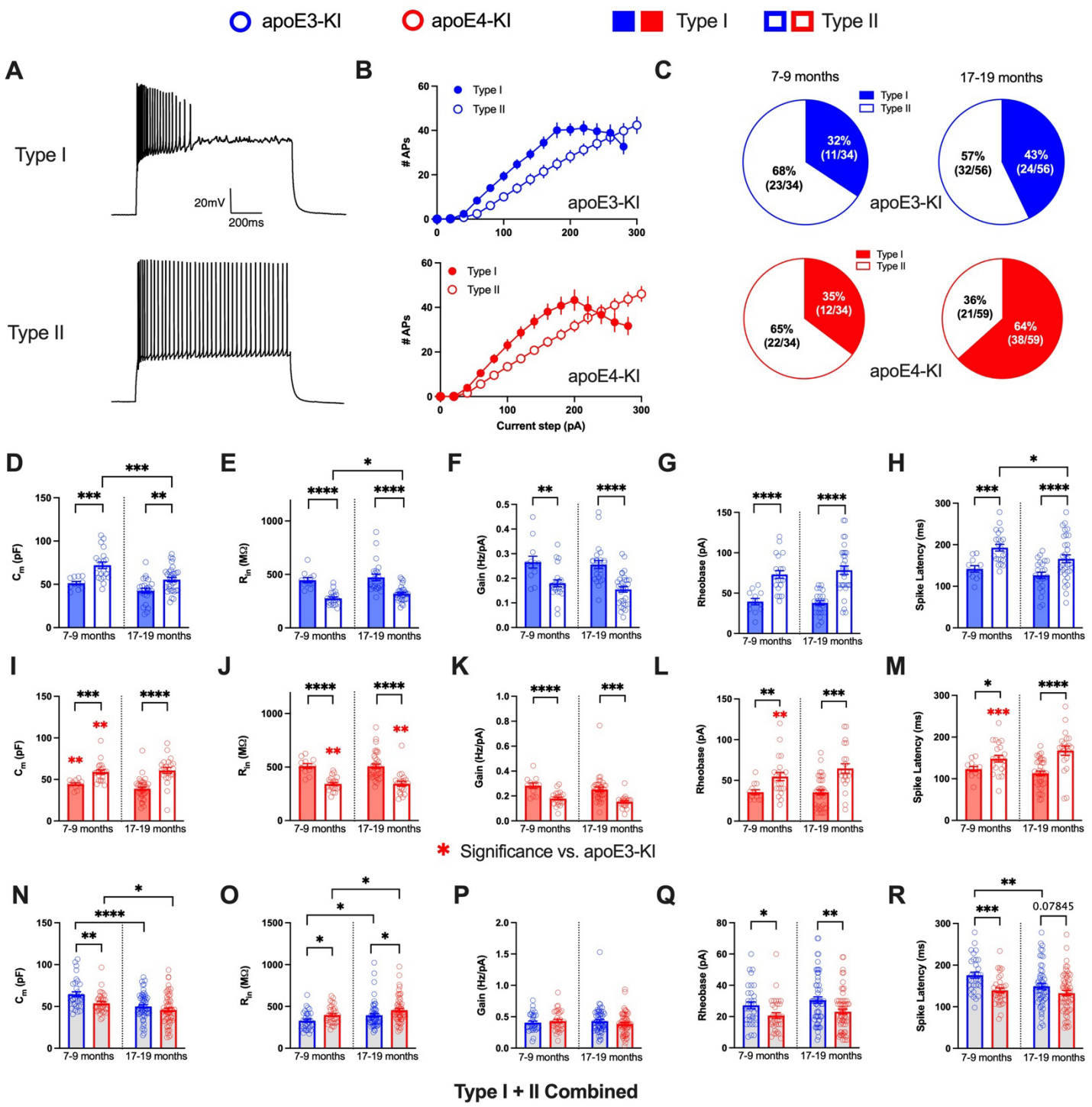

Figure 2. Dentate Gyrus granule cell (DGC) subpopulations display apoE genotype- and cell subtype-specific morpho-electric and excitability differences.

(A) Representative DGC firing traces in response to a 300pA 1-s depolarizing current injection.

(B) Input current – spike frequency relationships (I-F Curve) in DGCs from 7–9mo apoE3-KI (blue) and apoE4-KI (red) mice: the number of spikes elicited by 1 second epochs of incremental 20pA depolarizing current injections.

(C) Proportions of DGC subtypes in apoE3-KI (blue) and apoE4-KI (red) 7–9 and 17–19 month-old mice.

(D) C_m values for Type I (shaded bars) and Type II (clear bars) DGCs from 7–9 and 17–19 month-old apoE3-KI mice.

(E) R_{in} values for Type I and Type II apoE3-KI DGCs.

(F) Firing gain values for Type I and Type II apoE3-KI DGCs.

(G) Rheobase values for Type I and Type II apoE3-KI DGCs.

(H) Spike latency values for Type I and Type II apoE3-KI DGCs.

(I) C_m values for Type I and Type II DGCs from apoE4-KI mice. *Red asterisks indicate significant difference vs. corresponding parameter from age-matched apoE3-KI mice.

(J) R_{in} values for Type I and Type II apoE4-KI DGCs.

(K) Firing gain values for Type I and Type II apoE4-KI DGCs.

(L) Rheobase values for Type I and Type II apoE4-KI DGCs.

(M) Spike latency values for Type I and Type II apoE34-KI DGCs.

(N) C_m values for combined Type I and Type II DGCs from apoE3-KI and apoE4-KI mice.

(O) R_{in} values for combined Type I and Type II DGCs.

(P) Firing gain values for combined Type I and Type II DGCs.

(Q) Rheobase values for combined Type I and Type II DGCs.

(R) Spike latency values for combined Type I and Type II DGCs.

*$p<0.05$, **$p<0.01$, ***$p<0.001$, ****$p<0.0001$, unpaired two-tailed t-test or Mann-Whitney U test. N= 4 and 3 for DGCs from 7–9 month-old apoE3-KI and apoE4-KI mice, respectively; N= 5 each for DGCs from 17–19 month-old apoE3-KI and apoE4-KI mice. See also Supplementary Table 1.

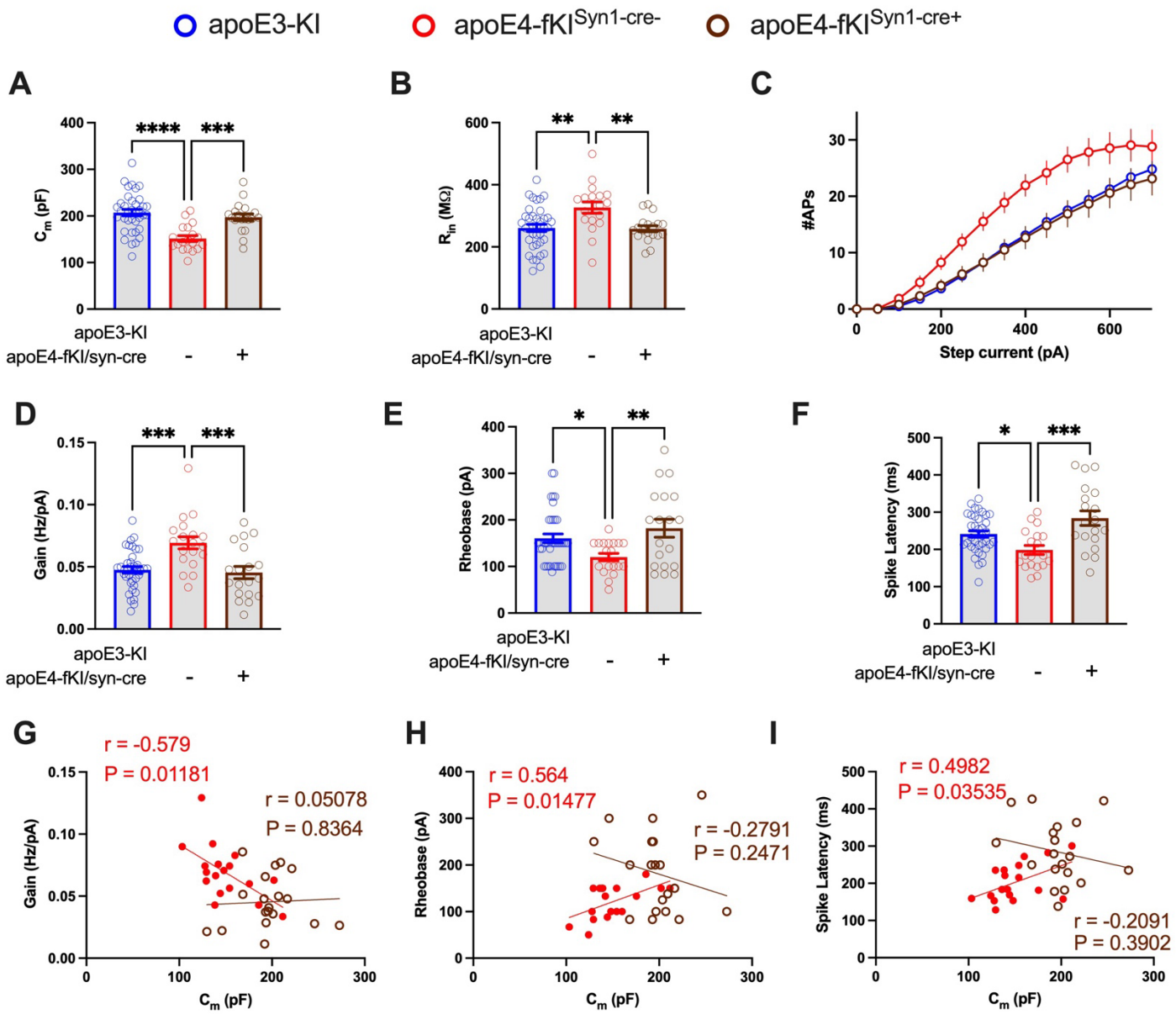

Figure 3. Selective apoE4 removal from neurons rescues morphological and excitability phenotype of CA3 PCs in young apoE4-fKI/Syn1-Cre mice.

Compared to their Cre-negative littermates that express apoE4 in neurons (red), 7–9mo apoE4-fKI/Syn1-Cre-positive mice (brown) displayed full normalization of all morpho-electric parameters to apoE3-KI levels (blue). apoE4-fKI/Syn1-Cre-positive neurons also showed abolished C_m - IE correlations, while apoE4-fKI/Syn1-Cre-negative neurons maintained these correlations.

(A) C_m values.

(B) R_{in} values.

(C) I-F curves.

(D) Firing gain values.

(E) Rheobase values.

(F) Spike latency values.

(G) C_m - Firing gain correlations.

(H) C_m – Rheobase correlations.

(I) C_m – Spike latency correlations.

*p<0.05, **p<0.01,***p<0.001,****p<0.0001, one-way ANOVA with Tukey's post-hoc multiple comparisons test. N = 3 each for apoE4-fKI/Syn1-Cre- and apoE4-fKI/Syn1-Cre+ mice. See also Supplementary Table 2.

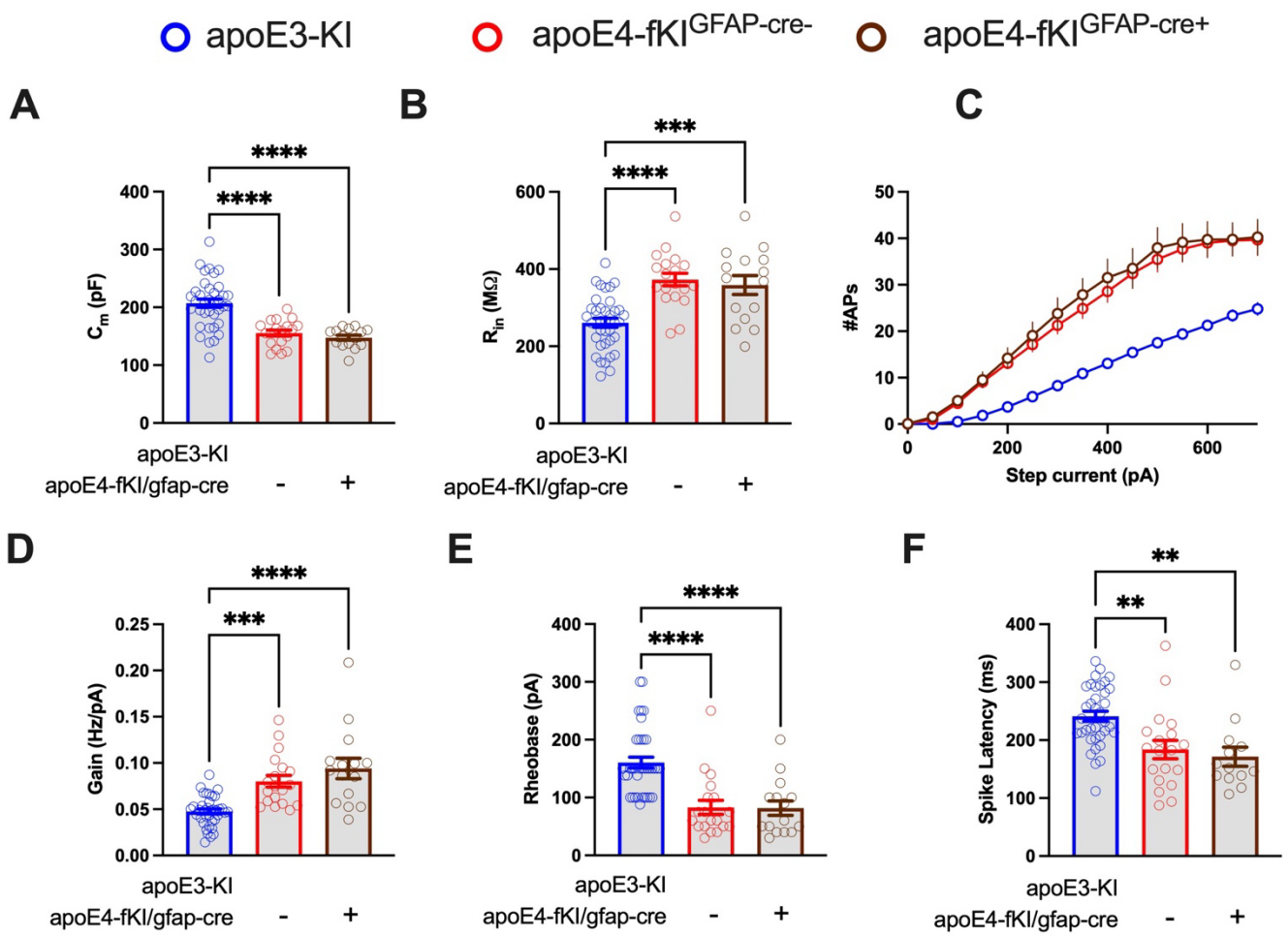

Figure 4. Selective apoE4 removal from astrocytes does not rescue morpho-electric or excitability phenotype of CA3 PCs in young apoE4-fKI/GFAP-Cre mice.

7–9-month-old apoE4-fKI/GFAP-Cre-positive mice (brown) displayed reduced cell size and hyperexcitable phenotype in CA3 PCs compared to neurons from age-matched apoE3-KI mice (blue) and showed no differences compared to their Cre-negative littermates that express apoE4 in astrocytes (red).

(A) C_m values.

(B) R_{in} values.

(C) I-F curves.

(D) Firing gain values.

(E) Rheobase values.

(F) Spike latency values.

p<0.01, ***p<0.001,**p<0.0001, one-way ANOVA with Tukey's post-hoc multiple comparisons test. N= 3 each for apoE4-fKI/GFAP-Cre- and apoE4-fKI/GFAP-Cre+ mice. See also Supplementary Table 2.

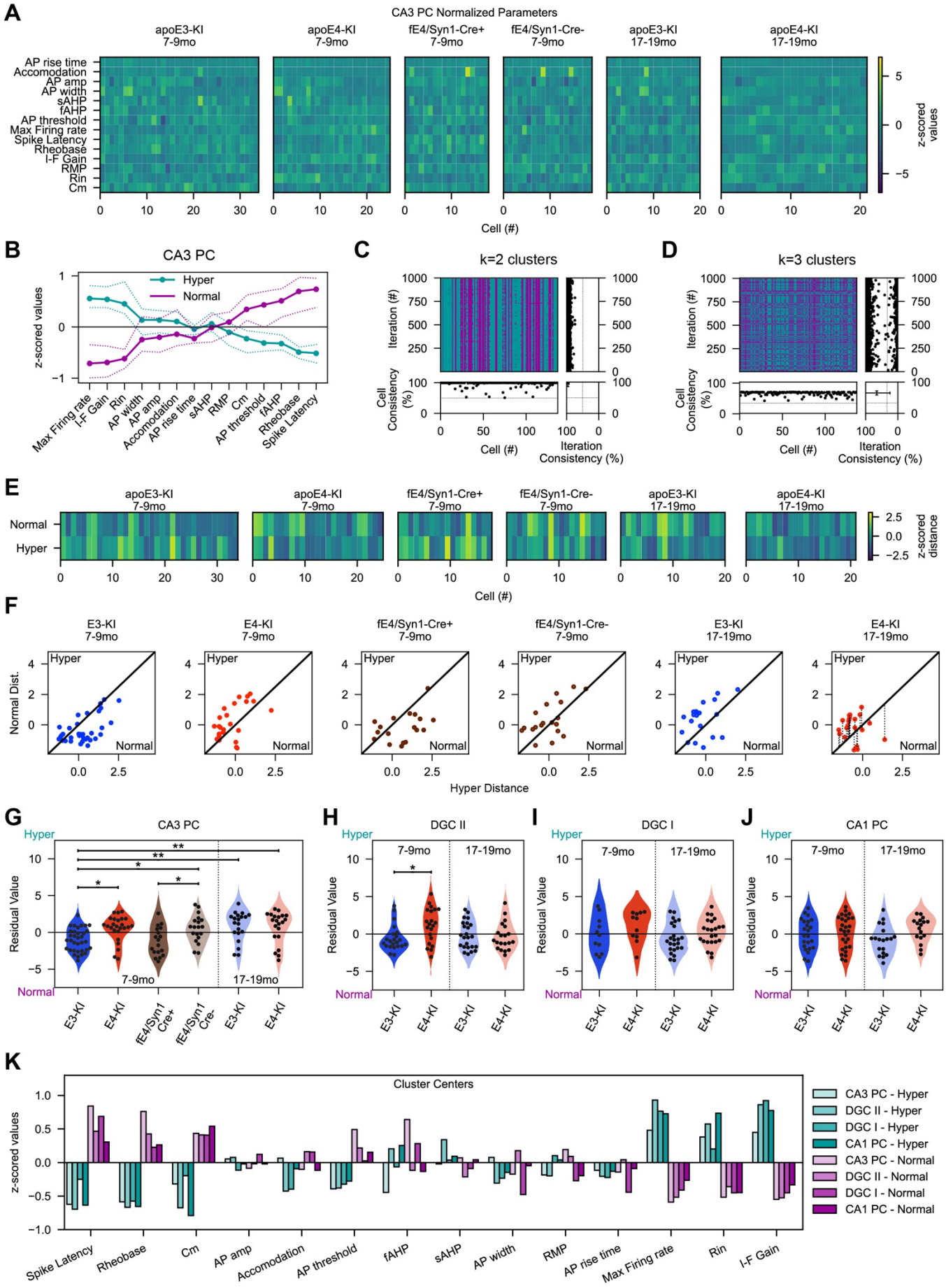
A
CA3 PC Normalized Parameters
apoE3-KI 7-9mo
apoE4-KI 7-9mo
fE4/Syn1-Cre+ 7-9mo
fE4/Syn1-Cre- 7-9mo
apoE3-KI 17-19mo
apoE4-KI 17-19mo
AP rise time
Accomodation
AP amp
AP width
sAHP
fAHP
AP threshold
Max Firing rate
Spike Latency
Rheobase
I-F Gain
RMP
Rin
Cm
z-scored values
Cell (#)
B
CA3 PC
Hyper
Normal
z-scored values
C
k=2 clusters
Iteration (#)
Cell Consistency (%)
Cell (#)
Iteration Consistency (%)
D
k=3 clusters
E
Normal
Hyper
z-scored distance
F
E3-KI 7-9mo
E4-KI 7-9mo
fE4/Syn1-Cre+ 7-9mo
fE4/Syn1-Cre- 7-9mo
E3-KI 17-19mo
E4-KI 17-19mo
Normal Dist.
Hyper Distance
G
CA3 PC
Residual Value
7-9mo
17-19mo
H
DGC II
I
DGC I
J
CA1 PC
K
Cluster Centers
z-scored values
CA3 PC - Hyper
DGC II - Hyper
DGC I - Hyper
CA1 PC - Hyper
CA3 PC - Normal
DGC II - Normal
DGC I - Normal
CA1 PC - Normal

Figure 5. Cluster analysis of CA3 pyramidal cells using k-means.

(A) Normalized cell parameters for CA3 pyramidal cells used for clustering analysis.

(B) Centroids from k-means with 2 clusters. Solid lines indicate the mean centroid after 1000 cross-validation iterations with dashed lines indicating the boot strapped 99% confidence interval. Cells divide into normal and hyperexcitable types. Morpho-electric parameters C_m and R_{in}, strongly associate with increased active metrics of excitability e.g. high firing rate gain and low rheobase.

(C) Cross validation of k-means sorting with k=2 clusters. Top left: Heat map showing the cluster label for each cell across all iterations. Top right: Raster showing consistency of labeling between full data set cluster and each iteration. Bottom left: Raster plot depicting consistency of labeling for each cell. Bottom right: Combined mean and standard deviation of cell and iteration consistency.

(D) Cross-validation as in (C) but with k=3 clusters.

(E) Distance from Normal and Hyperexcitable centroids for each cell group plotted as a heat map.

(F) Scatterplots for each cell depicting the normalized k-means distance from Normal and Hyperexcitable centroids. The decision line for clustering is the unity line plotted for each scatter plot. Right panel: the residuals for each cell are shown as dashed lines. Large positive residuals are more strongly associated with Hyperexcitable parameters while large negative residuals with Normal.

(G-J) Violin plots of the residual values for each hippocampal cell type, age group, and genotype.

(K) Centroid loadings for all cell types.

*$p<0.05$, **$p<0.01$, two-way ANOVA with post-hoc Tukey test.

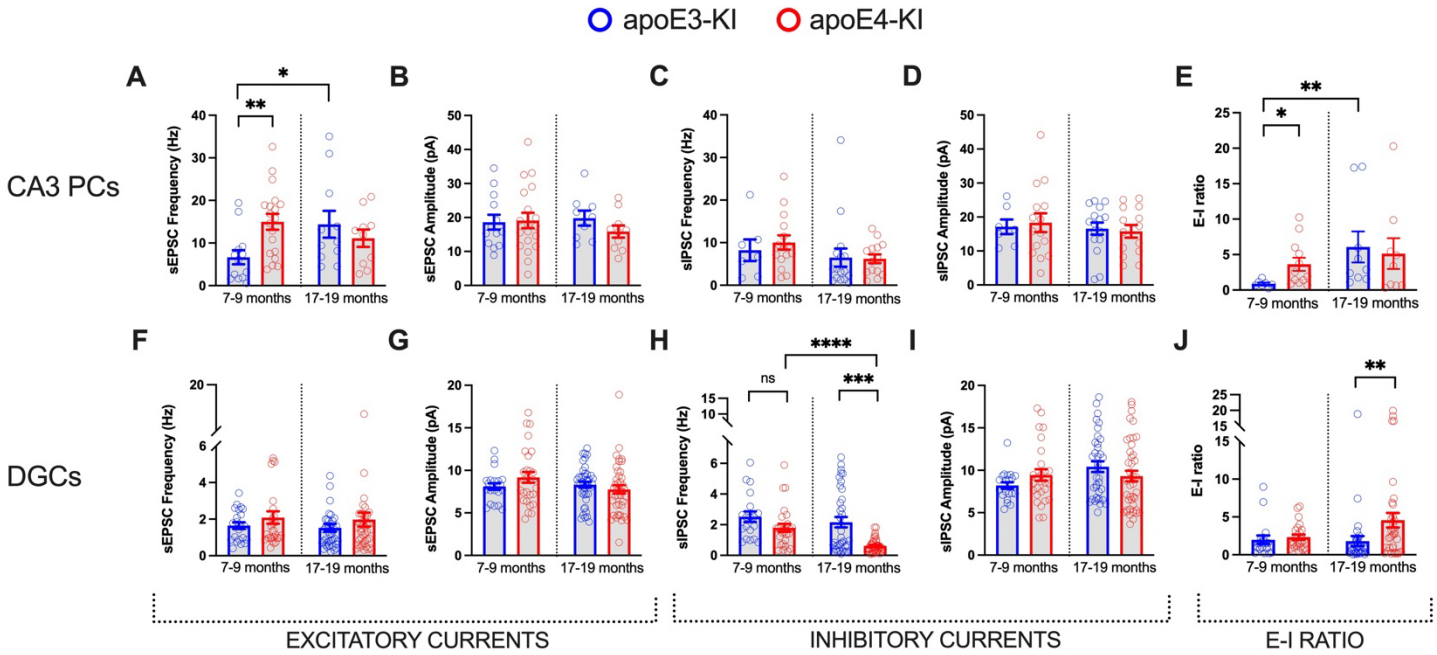

Figure 6. ApoE4-induced changes in spontaneous synaptic activity in CA3 and Dentate Gyrus.

(A) Spontaneous excitatory post-synaptic currents (sEPSC) frequency in CA3 PCs.

(B) sEPSC amplitudes in CA3 PCs.

(C) Spontaneous inhibitory post-synaptic currents (sIPSC) frequency in CA3 PCs.

(D) sIPSC amplitudes in CA3 PCs.

(E) Excitation-Inhibition (E-I) ratio in CA3 PCs.

(F) sEPSC frequency in DGCs.

(G) sEPSC amplitudes in DGCs.

(H) Spontaneous inhibitory post-synaptic currents (sIPSC) frequency in DGCs.

(I) sIPSC amplitudes in DGCs.

(J) Excitation-Inhibition (E-I) ratio in DGCs.

*p<0.05; **p<0.01, ***p<0.001, ****p<0.0001, unpaired two-tailed t-test or Mann-Whitney test. N= 5 and 6 mice for CA3 PCs from 7–9 month-old apoE3-KI and apoE4-KI mice, respectively; N= 6 for DGCs from 7–9 month-old apoE3-KI and apoE4-KI mice. N= 4–6 and 4–5 mice for CA3 PCs from 17–19 month-old apoE3-KI and apoE4-KI animals; N= 7 and 10 for DGCs from 17–19 month-old apoE3-KI and apoE4-KI mice, respectively. See also Figure S5 and Supplementary Table 3.

A

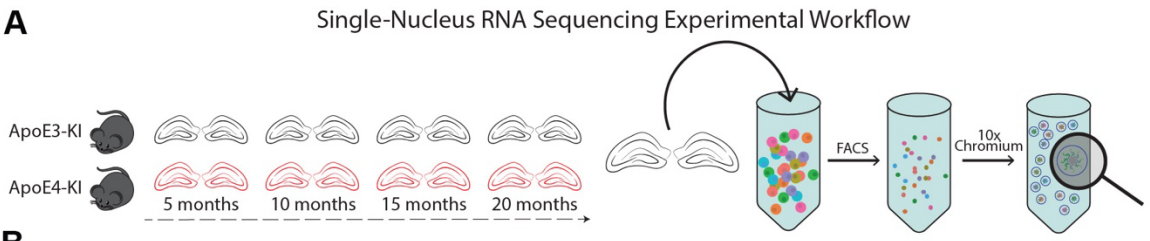

B

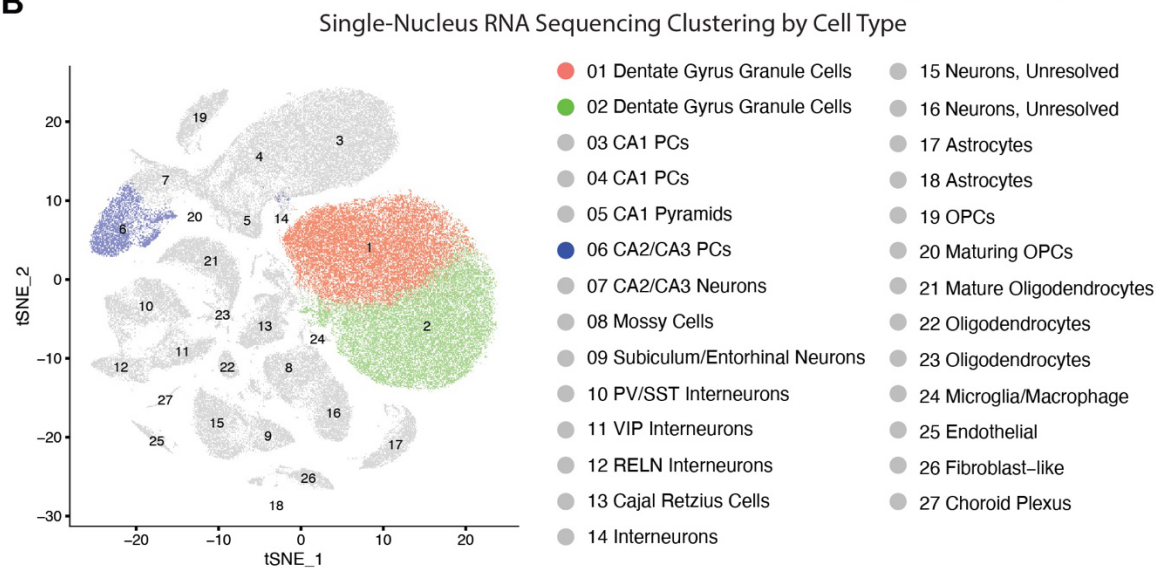

C

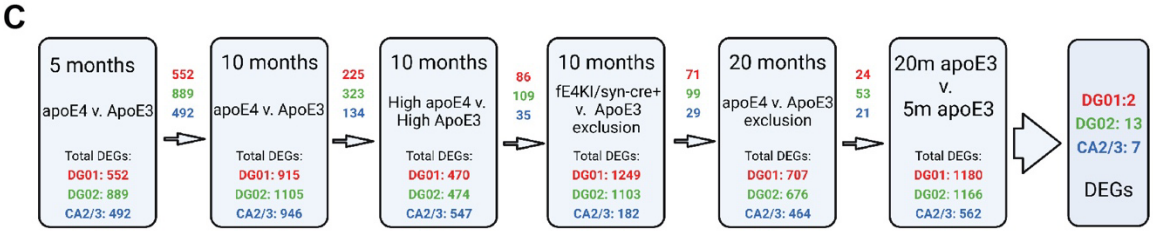

D

DG01

Gene	5 months		10 months		syn-cre 10 months		High E4 v. E3 @ 10m		Low E4 v. E3 @ 10m		20 months		E3 20m v. 5m	
	Log2FC	p-value	Log2FC	p-value	Log2FC	p-value	Log2FC	p-value	Log2FC	p-value	Log2FC	p-value	Log2FC	p-value
Mdga2	0.144	4.76E-06	0.167	2.57E-08	-	-	0.226	2.94E-02	0.162	2.07E-07	-	-	0.110711	7.87E-04
Tnrc6b	-0.129	3.93E-03	-0.215	5.82E-08	-	-	-0.379	8.63E-03	-0.201	1.06E-06	-	-	-0.085872	1.68E-03

E

DG02

Gene	5 months		10 months		syn-cre 10 months		High E4 v. E3 @ 10m		Low E4 v. E3 @ 10m		20 months		E3 20m v. 5m	
	Log2FC	p-value	Log2FC	p-value	Log2FC	p-value	Log2FC	p-value	Log2FC	p-value	Log2FC	p-value	Log2FC	p-value
Mdga2	0.103	4.84E-06	0.186	1.14E-16	-	-	0.308	1.80E-05	0.175	1.62E-13	-	-	0.086	1.58E-02
Lrrtm4	0.087	5.49E-11	0.258	0.00E+00	-	-	0.307	1.78E-11	0.253	0.00E+00	-	-	0.086	4.58E-07
Proca1	-0.082	4.04E-03	-0.117	1.25E-03	-	-	-0.357	2.18E-03	-0.095	1.53E-02			-0.137	7.57E-06
5330417C22Rik	-0.088	4.57E-02	-0.176	1.55E-06	-	-	-0.333	1.58E-02	-0.161	1.83E-05	0.056	9.82E-01	-0.076	7.12E-03
Clta	-0.127	2.27E-03	-0.082	1.61E-02	-	-	-0.314	4.18E-02	0.000	0.00E+00	-	-	-0.103	5.87E-04
Chst9	-0.126	4.01E-03	-0.273	3.86E-17	-	-	-0.305	1.50E-03	-0.269	4.87E-15	-	-	-0.102	2.03E-03
Cyp7b1	-0.127	4.18E-04	-0.136	2.84E-05	-	-	-0.290	6.69E-03	-0.121	3.87E-04	-	-	-0.118	3.08E-04
Creld1	-0.082	1.02E-02	-0.147	2.23E-05	-	-	-0.278	6.89E-03	-0.135	3.46E-04	-	-	-0.071	9.70E-04
Rph3al	-0.136	5.96E-04	-0.176	8.04E-08	-	-	-0.253	3.51E-02	-0.169	6.55E-07	-	-	-0.174	4.25E-07
Nell2	0.105	3.94E-05	0.155	1.06E-08	-	-	0.203	3.85E-02	0.150	8.87E-08	-	-	0.101	8.42E-03
Ubn2	-0.117	1.70E-04	-0.071	2.69E-02	-	-	-0.227	4.97E-02	0.000	0.00E+00	-	-	-0.159	7.29E-06
Plxna4	-0.117	5.13E-06	-0.191	3.94E-18	0.072	5.51E-02	-0.209	3.92E-03	-0.190	2.18E-16	-	-	-0.092	9.97E-04
Parvb	-0.070	1.11E-02	-0.075	1.38E-02	-	-	-0.185	4.74E-02	0.000	0.00E+00	-	-	-0.077	1.78E-03

F

CA2/3 PCs

Gene	5 months		10 months		syn-cre 10 months		High E4 v. E3 @ 10m		Low E4 v. E3 @ 10m		20 months		E3 20m v. 5m	
	Log2FC	p-value	Log2FC	p-value	Log2FC	p-value	Log2FC	p-value	Log2FC	p-value	Log2FC	p-value	Log2FC	p-value
Nell2	0.058	3.22E-02	0.236	2.64E-05	-	-	0.457	4.14E-04	0.206	1.32E-03	-	-	0.123	1.66E-03
Rnf182	-0.327	3.17E-04	-0.260	1.45E-03	-	-	-0.647	3.01E-03	-0.211	2.34E-02	1.053	4.31E-01	-0.353	6.64E-05
Dclk1	0.202	7.84E-04	0.182	1.10E-04	-	-	0.406	4.91E-03	0.153	1.62E-03	0.952	4.89E-01	0.204	7.46E-03
Slit3	0.142	8.37E-03	0.280	5.02E-07	-0.1215	4.40E-01	0.396	1.63E-02	0.260	1.03E-05	0.940	1.77E-01	0.294	3.46E-07
Ppfia2	0.133	5.88E-03	0.213	2.01E-04	0.0718	1.85E-01	0.377	2.83E-03	0.191	2.98E-03	0.951	2.42E-01	0.172	2.09E-03
Lrrc7	0.199	3.39E-04	0.114	1.51E-04	-	-	0.192	3.99E-02	0.104	8.67E-04	1.046	9.55E-02	0.105	2.70E-02
Nlgn1	0.106	1.42E-02	0.054	4.95E-03	-0.2121	7.18E-02	0.147	3.51E-02	0.000	0.00E+00	-	-	0.070	3.52E-02

Figure 7. snRNA-seq analysis of apoE3-KI and apoE4-KI mouse hippocampi at different ages.

(A) Experimental design: hippocampi were extracted from female apoE3-KI and apoE4-KI mice at 5, 10, 15 and 20 months of age (*n*=4 per genotype and age). The hippocampi were dissociated, and nuclei were labeled with DAPI and isolated using flow cytometry before processing using the 10x Chromium v2 system for snRNA-seq.

(B) Clustering using the Seurat package revealed 27 distinct cellular populations. Marker gene analysis led to the identification of 16 neuronal clusters (Clusters 1–16) and 11 non-neuronal clusters (Clusters 17–27).

(C) Selection criteria for clusters 1, 2, and 6. Values represent the number of genes passing each successive criteria.

(D) Cell type- and age- specific differentially expressed genes whose expression pattern fits the criteria shown in (C) for cluster DG01. Gene selected for further CRISPRi confirmation (Mdga2) is highlighted in red.

(E) Differentially expressed genes for DG02 cluster. Genes selected for further CRISPRi confirmation (Mdga2 and Nell2) are highlighted in red.

(F) Differentially expressed genes for CA2/3 PC cluster. Gene selected for further CRISPRi confirmation (Nell2) is highlighted in red.

See also Supplementary Tables 5-7.

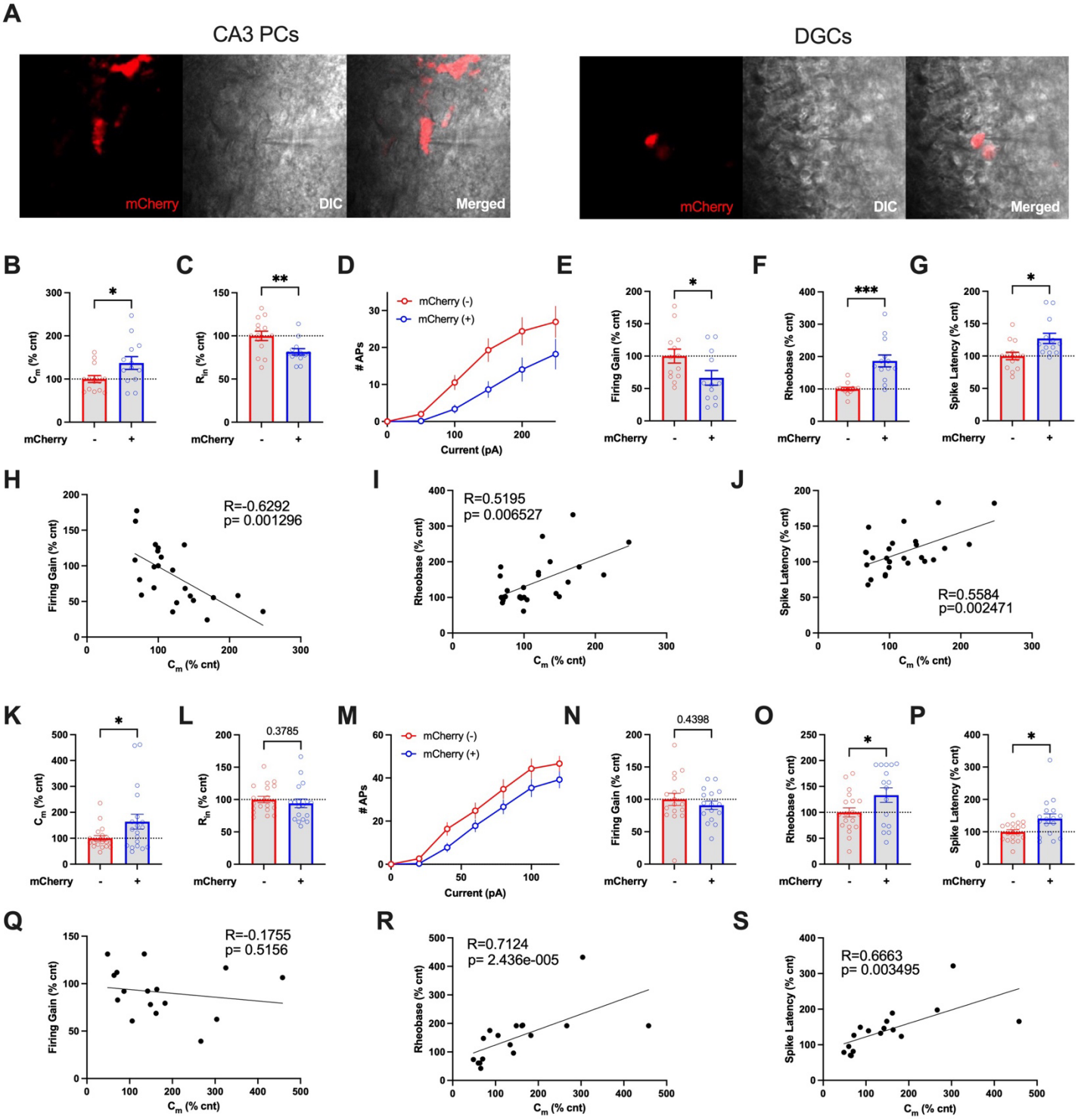

Figure 8. CRISPRi-induced reduction in Nell2 expression normalizes size and excitability of transduced CA3 pyramidal cells and dentate granule cells from young apoE4-KI mice.

(A) Example images of transduced cells expressing mCherry (red, left panels) targeted for whole-cell patch recording in acute brain slices under differential interference contrast (DIC) imaging (middle panels). Right panels: overlay.

(B) Membrane capacitance (C_m) values for mCherry- and mCherry+ CA3 PCs, normalized to mCherry- average for each slice.

(C) Input resistance (R_{in}) values for mCherry- and mCherry+ CA3 PCs, normalized to mCherry- average for each slice.

(D) Input current – firing rate relationships (I-F Curves), the average number of spikes elicited by incremental depolarizing current injections.

(E) Firing gain values, quantified as the linear slope of the I-F curve, normalized to mCherry- average for each slice.

(F) Rheobase values in CA3 PCs normalized to mCherry- average for each slice.

(G) Spike latency values in CA3 PCs normalized to mCherry- average for each slice.

(H-J) Increase in C_m correlates with reduction in excitability in all recorded CA3 PCs:

(H) C_m - Firing gain correlation for CA3 PCs.

(I) C_m – Rheobase correlation for CA3 PCs.

(J) C_m - Spike Latency correlation for CA3 PCs.

(K) Membrane capacitance (C_m) values for mCherry- and mCherry+ DGCs, normalized to mCherry- average for each slice**.**

(L) Input resistance (R_{in}) values for mCherry- and mCherry+ DGCs, normalized to mCherry- average for each slice.

(M) I-F Curves for DGCs.

(N) Firing gain values in DGCs normalized to mCherry- average for each slice. Lack of rescue in this parameter is consistent lack of apoE4-induced firing gain phenotype in these neurons (see Figure 1).

(O) Rheobase values in DGCs normalized to mCherry- average for each slice.

(P) Spike latency values in DGCs normalized to mCherry- average for each slice.

(Q) C_m -Firing gain correlation for DGCs (mCherry+ cells showed no changes in this parameter, see N),

(R) C_m - Rheobase correlation for DGCs.

(S) C_m - spike latency correlation for DGCs.

*$p<0.05$, **$p<0.01$, ***$p<0.001$, unpaired two-tailed t-test or Mann-Whitney U test, and Pearson r test. N= 5 and 4 mice for CA3 PCs and DGCs, respectively. See also Supplementary Table 4.

Lead contact

Further information and requests for resources or reagents should be directed to and will be fulfilled by the lead contact, Misha Zilberter (misha.zilberter@gladstone.ucsf.edu).

Materials availability

Materials generated during this study are accessible via reasonable request to the corresponding authors' labs.

Data and code availability

All data associated with this study and the information of used materials are available in the main text, the Materials and Methods, or the Supplementary Information section. Data associated with all figures, Supplementary Tables and Supplementary Figures are also available in the Supplementary Information. All code used in this study is accessible via reasonable request to the corresponding authors' labs.

EXPERIMENTAL MODEL DETAILS

Study Design

The first objective of this study was to investigate the neuronal electrophysiological dysfunction as the mechanism of apoE4- versus apoE3-driven network pathogenesis in AD. We performed functional electrophysiological characterization of excitatory hippocampal neurons from female mice expressing human apoE4 or apoE3 at two ages of 7-9 and 17-19 months. To confirm the role of neuronal apoE4 expression we used genetically modified mice with apoE4 selectively deleted from neurons or astrocytes. The second objective of the study was to uncover the apoE4-induced neuronal transcriptomic changes responsible for the observed functional deficits. We analyzed single-nucleus RNA sequencing (snRNA-seq) data from our previous study to find the genes whose apoE genotype- and age- dependent expression differences matched the observed morpho-electric phenotype. We confirmed the selected differentially expressed genes' role by CRISPRi intervention. Sample sizes were chosen on the basis of previous results to allow for adequate statistical power. Mice were matched for age and gender. Researchers were blinded to mouse genotype to exclude the possibility of bias. For specific experiments, refer to the relevant Materials and Methods section and figure legends for outcome measures, statistical methods, and experimental procedures.

Mice

Human apoE3-KI and apoE4-KI mice[93] were from Taconic. LoxP-floxed apoE knock-in (apoE-fKI) mice were generated as described previously[94]. Mice with a conditional deletion of the human *APOE* gene were created as described previously[38]: homozygous apoE3-fKI (apoE3/3) and apoE4-fKI (apoE4/4) mice were crossbred with

GFAP-Cre transgenic mice [B6.Cg-Tg(GFAP-cre)8Gtm][95,96] or Synapsin 1-Cre (Syn-1-Cre) transgenic mice [B6.Cg-Tg(Syn1-cre)671Jxm/J][97]. These lines produced mice that were heterozygous for apoE3 or apoE4 and positive for GFAP-Cre or Syn-1-Cre. These mice were crossbred with homozygous apoE3-fKI or apoE4-fKI mice to generate mice that were homozygous for apoE3 or apoE4 and positive for GFAP-Cre (apoE-fKI$^{GFAP\text{-}Cre}$) or Syn-1-Cre (apoE-fKI$^{Syn1\text{-}Cre}$). Littermates negative for GFAP-Cre or Syn-1-Cre were used as controls. All mice were on a pure C57BL/6 genetic background and were housed in a pathogen-free barrier facility on a 12 h light cycle at 19-23ºC and 30-70% humidity. Animals were identified by ear punch under brief isoflurane anesthesia and genotyped by polymerase chain reaction (PCR) of a tail clipping. All animals otherwise received no procedures except those reported in this study. All animal experiments were conducted in accordance with the guidelines and regulation of the National Institutes of Health, the University of California, and the Gladstone Institutes under the protocol AN176773

Viral Injections

For viral transduction, 5-month-old female mice anesthetized with an initial intraperitoneal (IP) injection of ketamine/xylazine mix, and maintained with 1% isoflurane oxygen mix at a flow rate of one liter per minute. The scalp area was cleaned and hair chemically removed. A small incision in the scalp was made to reveal the midline suture from bregma to lambda. Using a stereotactic frame equipped with a small high-speed drill 0.5mm burr holes were drilled through the skull at coordinates 2.1mm posterior to bregma and ±1.5mm lateral to the midline, at a depth to reveal the surface of the cortex. A 28 gauge canula attached to a syringe pump was lowered to a depth of 1.5mm below the cortical surface and 2uL of lentivirus was injected at a rate of 500nL/min. After each delivery we waited an additional 2 minutes for pressure equalization before the canula was slowly removed. The scalp was sutured closed with silk thread. At the end of surgery mice were treated with subcutaneous ketofen injection near the incision site, an IP injection of buprenorphine and one of saline for hydration. Mice were allowed to recover in new cages warmed by a heating pad. At the end of the four-hour recovery a second injection of buprenorphine was administered and cages were returned to primary housing racks.

Tissue slice preparation

Mice were deeply anesthetized with isoflurane and decapitated. The brain was rapidly removed from the skull and placed in the 4°C slicing solution comprised of 110 mM Choline Chloride, 2.5 mM KCl, 1.25 mM NaH_2PO_4, 26 mM $NaHCO_3$, 2 mM $CaCl_2$, 1.3 mM Na Pyruvate, 1 mM L-Ascorbic Acid, and 10 mM dextrose. 300µm sagittal or horizontal sections were cut using a vibratome (VT 1200s, Leica). Following slicing, slices were transferred into a vapor interface holding chamber (Scientific Systems Design Inc, Canada) aerated with 95% O_2/5% CO_2 gas mixture and allowed to recover at 34°C for 1 h before recording.

Whole-cell patch clamp electrophysiology

Brain slices were placed into a submerged dual-side recording chamber (RC-27D, Warner Scientific) and perfused at 7 mL/min with oxygenated ACSF solution at 34°C. Recording and holding ACSF solution was comprised of 124mM NaCl, 26mM $NaHCO_3$, 10mM Glucose, 1.25mM NaH_2PO_4, 2.5mM KCl, 1.25mM $MgCl_2$, and 1.5mM $CaCl_2$.

Neurons were imaged using a modified Olympus BXW-51 microscope with a 60x objective (Scientifica Inc, Great Britain). Whole-cell patch-clamp recordings were performed using a Multiclamp 700B amplifier with signals sampled at 10 kHz and digitized using a Digidata 1550B with Axon pCLAMP software (all from Molecular Devices, USA).

Intrinsic neuronal excitability and passive parameter measurements. Cells were allowed to stabilize for minimum of 3 minutes after obtaining whole-cell patch configuration before recordings commenced. Patch pipettes were filled with potassium-gluconate based solution containing 122.5 mM K-gluconate, 8 mM KCl, 10 mM HEPES, 2 mM $MgCl_2$, 0.2 mM EGTA, 2 mM ATPNa, and 0.3 mM GTPNa, pH set to 7.2–7.3 with KOH and with osmolarity of 270-280 mOsm. To block spontaneous synaptic activity, AMPA receptor antagonist 6-cyano-7-nitroquinoxaline-2,3-dione (CNQX, 20μM), NMDA receptor antagonist D-(–)-2-amino-5-phosphonopentanoic acid (AP-5, 50μM) and $GABA_A$ receptor antagonist Picrotoxin (5μM) were added to the perfusate.

Cell membrane capacitance (C_m). C_m was measured in voltage clamp configuration at -70mV using Clampex software's Membrane Test protocol as the integral of the fast capacitance transient current resulting from a 10mV, 5ms square pulse stimulation.

Input resistance (R_{in}). R_{in} was measured in current clamp configuration at V_m of -70mV using 1s, 10pA current injections from -50 to +50pA. Resulting I-ΔV_m curve was fitted with a linear slope to calculate the input resistance. *Resting Membrane Potential* was measured in current clamp configuration at I=0.

Input current-Spiking Frequency (I-F). I-F relationship was recorded in current clamp configuration using incremental 1-s 20pA (CA1 PCs and DGCs) or 50pA (CA3 PCs) depolarizing current injections at 0.1Hz with resting membrane potential held at -70mV. Resulting spike count was then plotted against the current step magnitude to generate the I-F curve.

Firing gain. Firing gain was calculated as the linear slope of the first 5 steps in the I-F curve starting from rheobase.

Rheobase. Rheobase was determined from -70mV as the minimum magnitude of the 1s depolarizing current injection required to elicit an action potential.

Spike latency. Spike latency was measured in current clamp configuration at -70mV using a 1s 800pA current ramped injection, as the delay from the beginning of the stimulation to the generation of the first action potential (when dV_m reached 20V/s).

Accommodation. Accommodation was measured as the ratio of last to first interspike interval in response to a 1s step current injection at twice the rheobase.

Action potential threshold*.* Action potential threshold was measured at rheobase step as the V_m value where dV_m crossed 20V/s.

Fast afterhypolarization (fAHP). fAHP was measured as a negative-going peak following the action potential relative to the action potential threshold under a 1s current step injection that elicited at least 4 action potentials.

Slow afterhypolarization (sAHP). sAHP was measured as the negative-going peak relative to baseline within a 1s period immediately after 1s 300pA current step injection.

Spontaneous synaptic activity recording. Postsynaptic currents were recorded using a Cs^+-based intracellular pipette solution containing: 140mM $CsMeSO_4$, 10mM HEPES, 2mM $MgCl_2$, 0.6mM EGTA, 2mM ATPNa, 0.3mM GTPNa, set to pH 7.2–7.3 with CsOH and with osmolarity of 270-280 mOsm. Spontaneous excitatory postsynaptic currents (sEPSCs) were recorded at -70mV, inhibitory postsynaptic currents (sIPCSs) at 0mV, for a period of 3-5 minutes.

Single-nucleus RNA sequencing

snRNA-seq dataset from the previous publication[40] (GEO accession: GSE167497) was used for the analysis in the current study.

Pre-processing and clustering of mouse snRNA-seq samples. Clustering was performed following a previously established method[40]. Demultiplexed FASTQ files were aligned to a custom reference genome built from mm10-1.2.0, which includes introns. This alignment was conducted using the Cell Ranger v2.0.1 counts function with default parameters, as outlined in the Cell Ranger documentation. UMI counts were also determined using the Cell Ranger counts function, and count matrices from multiple samples were merged into a single count matrix using Cell Ranger's aggr function with default parameters. Barcodes (potential cells) were filtered based on a UMI count threshold. The filtered UMI count matrices were further processed using Seurat v2.3.4. Specifically, the data were filtered to include only protein-coding genes. Cells were filtered to include only those with 200-2,400 detected genes, 500-4,500 UMIs, and less than 0.25% mitochondrial reads, ensuring data quality. This quality control process resulted in a final matrix of 21,204 genes by 123,489 nuclei. To normalize the gene expression matrices, the Seurat NormalizeData function[98,99] was employed with a scale factor of 10,000. Clustering was performed using the implementation in Seurat v2.3.4. This algorithm involved embedding cells in a k-nearest neighbor graph based on Euclidean distance in PCA space. The edge weights between cells were refined using Jaccard similarity. The Louvain algorithm was used for clustering. Highly dispersed genes

were identified using the Seurat FindVariableGenes function[98,99]. These genes were selected based on an average expression range of 0.25-4 and a minimum dispersion of 0.55, resulting in a list of 2,197 genes. Nearest neighbor distances were computed using up to the first 15 principal components and a resolution of 0.6, leading to the identification of 27 distinct clusters.

Cell type assignment. Cell type assignment was done as described previously[40]: The t-SNE data visualization technique was used to examine the presence of clusters in which mouse ages and genotypes were intermingled, without any observable indications of batch effects associated with genotype or age. To identify marker genes for each cluster, the FindAllMarkers function in Seurat[98,99] was utilized. This algorithm uses the Wilcoxon rank-sum test to iteratively compare gene expression within a putative cluster against the expression in all other clusters. Marker genes were selectively chosen to exhibit positive expression (i.e., higher expression in the cluster of interest compared to other clusters), to be detected in at least 10% of cells within the cluster, and to demonstrate a 0.25 log2 fold higher expression in the cluster of interest relative to other clusters. To determine broad cell classes, including excitatory and inhibitory neurons, astrocytes, oligodendrocytes, and OPCs, marker genes were compared against cell-type-specific markers obtained from previous RNA sequencing data on sorted cell types[100]. Moreover, for further subdivision of hippocampal cell types, particularly in the identification of principal cell subsets, marker genes for each cluster were compared against hippocampal cell-type-specific marker genes reported in hipposeq[101]. In the case of less common non-neuronal cell types, we compared gene expression in our cells with those genes enriched in each hippocampal cell type relative to all other cells in the hippocampus, as described in the DropViz resource[102]. To further corroborate the identity of the clusters, we additionally queried the top marker genes for each cluster against the Allen Brain's genome-wide atlas of gene expression in the adult mouse brain[103].

Differential Gene Expression. To find genes that matched the selection criteria of interest based on the significant effects in our morpho-electric data, a set of differential gene expression tests were done between cell populations of interest. Statistically significant DEGs were detected using the non-parameteric Wilcoxon rank sum test, which was implemented using the FindMarkers function in Seurat. Only genes that are detected in a minimum fraction of 0.1 in either cell population were considered. A differential expression level threshold of absolute logFC = 0.05 was used. The p-value was adjusted based on bonferroni correction. Genes with adjusted p-value < 0.05 were considered significantly differentially expressed. For the combined analysis of multiple differential expression comparisons, genes matching the differential expression criteria across multiple comparisons were chosen for further analysis.

CRISPRi vector design

dCas9/KRAB-mediated CRISPRi vectors for Nell2 and Mdga2 were custom designed, produced and packaged into lentivirus by VectorBuilder (USA) using previously published methods[51,104,105]. Specifically, multiple CRISPRi sgRNA sequences were designed for each target gene using VectorBuilder's algorithm. For each target, two

sgRNAs were chosen based on their off-target potential, proximity to the transcript start area, and sequence characteristics (excluding sequences with consecutive Cs and Gs). They were constructed into a lentivirus vector for the CRISPRi application.

Data analysis and statistics

Electrophysiological data analysis was done in Igor Pro 8 (Wavemetrics Inc, USA) using custom scripts. Postsynaptic events were quantified using a template matching algorithm in NeuroMatic v.3c plug-in for Igor Pro (Jason Rothman).

K-means clustering analysis. Cluster analysis was performed using python (v3.10.12) scripts. For each cell type, clustering was performed with ages and genotypes combined. Electrophysiological measures were normalized in to z-scores. The K-means clustering algorithm[106] implemented by the Scikit-learn package[107] was applied to the complete set of normalized data as well as 1000 iterations using randomly selected 80:20 train:test holdout method. This cross validation was performed at 2 and 3 clusters to estimate the robustness of the classification paradigm. To calculate strength of membership residuals, the distances from each centroid determined by the k-means algorithm were normalized to z-scores, and for each cell the difference (residual) in distances were used to estimate the affinity for Hyperexcitable or Normal clusters. These residuals for different genotypes and ages were compared with two-way ANOVAs and pos-hoc Tukey tests.

Statistical analysis. Statistical analysis was performed using Prism 9 software (GraphPad Software LLC). Maximum Likelihood Test and false discovery rate correction were performed using custom scripts in python using the Scikit-learn[107] and statsmodels[108] packages. Exact statistical tests used are specified in figure legends. The rest of the statistical details including mean, SEM, n (number of recorded cells), N (number of mice per group), FDR and p values are included in Supplementary Tables 1-4.

Supplementary Tables

Supplementary Table 1. Detailed information on all neuronal parameters from apoE4-KI mice presented in Figures 1, 2, and S1-3.
Supplementary Table 2. Detailed information on all neuronal parameters for apoE4-fKI mice presented in Figures 3+4
Supplementary Table 3. Detailed information on all synaptic activity recordings in apoE-KI mice presented in Figure 6.
Supplementary Table 4. Detailed information on all neuronal parameters from CRISPRi experiments in apoE4-KI mice presented in Figures 8 and S6.
Supplementary Table 5. List of all differentially expressed genes for DGC01 cluster shown in Figure 7.
Supplementary Table 6. List of all differentially expressed genes for DGC02 cluster shown in Figure 7.
Supplementary Table 7. List of all differentially expressed genes for CA2/3PC cluster shown in Figure 7.

References

1. Corder, E.H., Saunders, A.M., Strittmatter, W.J., Schmechel, D.E., Gaskell, P.C., Small, G.W., Roses, A.D., Haines, J.L., and Pericak-Vance, M.A. (1993). Gene dose of apolipoprotein E type 4 allele and the risk of Alzheimer's disease in late onset families. Science *261*, 921–923.

2. Saunders, A.M., Schmader, K., Breitner, J.C., Benson, M.D., Brown, W.T., Goldfarb, L., Goldgaber, D., Manwaring, M.G., Szymanski, M.H., and McCown, N. (1993). Apolipoprotein E epsilon 4 allele distributions in late-onset Alzheimer's disease and in other amyloid-forming diseases. Lancet *342*, 710–711.

3. Farrer, L.A., Cupples, L.A., Haines, J.L., Hyman, B., Kukull, W.A., Mayeux, R., Myers, R.H., Pericak-Vance, M.A., Risch, N., and Duijn, C.M. van (1997). Effects of age, sex, and ethnicity on the association between apolipoprotein E genotype and Alzheimer disease. A meta-analysis. APOE and Alzheimer Disease Meta Analysis Consortium. JAMA *278*, 1349–1356.

4. Caselli, R.J. (2009). Age-related memory decline and apolipoprotein E e4. Discov Med *8*, 47–50.

5. Shaw, P., Lerch, J.P., Pruessner, J.C., Taylor, K.N., Rose, A.B., Greenstein, D., Clasen, L., Evans, A., Rapoport, J.L., and Giedd, J.N. (2007). Cortical morphology in children and adolescents with different apolipoprotein E gene polymorphisms: an observational study. Lancet Neurol *6*, 494–500. 10.1016/s1474-4422(07)70106-0.

6. Nao, J., Sun, H., Wang, Q., Ma, S., Zhang, S., Dong, X., Ma, Y., Wang, X., and Zheng, D. (2017). Adverse Effects of the Apolipoprotein E ε4 Allele on Episodic Memory, Task Switching and Gray Matter Volume in Healthy Young Adults. Front Hum Neurosci *11*, 346. 10.3389/fnhum.2017.00346.

7. Bookheimer, S.Y., Strojwas, M.H., Cohen, M.S., Saunders, A.M., Pericak-Vance, M.A., Mazziotta, J.C., and Small, G.W. (2000). Patterns of brain activation in people at risk for Alzheimer's disease. N Engl J Med *343*, 450–456. 10.1056/nejm200008173430701.

8. Pihlajamäki, M., and Sperling, R.A. (2009). Functional MRI assessment of task-induced deactivation of the default mode network in Alzheimer's disease and at-risk older individuals. Behav Neurol *21*, 77–91. 10.3233/ben-2009-0231.

9. Haberman, R.P., Branch, A., and Gallagher, M. (2017). Targeting Neural Hyperactivity as a Treatment to Stem Progression of Late-Onset Alzheimer's Disease. Neurotherapeutics *14*, 662–676. 10.1007/s13311-017-0541-z.

10. Palop, J.J., and Mucke, L. (2016). Network abnormalities and interneuron dysfunction in Alzheimer disease. Nat. Rev. Neurosci. *17*, 777–792. 10.1038/nrn.2016.141.

11. Sanchez, P.E., Zhu, L., Verret, L., Vossel, K.A., Orr, A.G., Cirrito, J.R., Devidze, N., Ho, K., Yu, G.-Q., Palop, J.J., et al. (2012). Levetiracetam suppresses neuronal network dysfunction and reverses synaptic and cognitive deficits in an Alzheimer's disease model. Proceedings of the National Academy of Sciences *109*, E2895-903. 10.1073/pnas.1121081109.

12. Canter, R.G., Penney, J., and Tsai, L.-H. (2016). The road to restoring neural circuits for the treatment of Alzheimer's disease. Nature *539*, 187–196. 10.1038/nature20412.

13. Palop, J.J., and Mucke, L. (2009). Epilepsy and cognitive impairments in Alzheimer disease. Archives of Neurology *66*, 435–440. 10.1001/archneurol.2009.15.

14. Diaz-Arrastia, R., Gong, Y., Fair, S., Scott, K.D., Garcia, M.C., Carlile, M.C., Agostini, M.A., and Ness, P.C.V. (2003). Increased risk of late posttraumatic seizures associated with inheritance of APOE epsilon4 allele. Archives of Neurology *60*, 818–822. 10.1001/archneur.60.6.818.

15. Harden, C.L. (2004). The Apolipoprotein E Epsilon (epsilon) 4 Allele Is Important for Trauma-related Epilepsy. Epilepsy Curr *4*, 29–30. 10.1111/j.1535-7597.2004.04112.x.

16. Sporiš, D., Sertic, J., Henigsberg, N., Mahovic, D., Bogdanovic, N., and Babic, T. (2005). Association of refractory complex partial seizures with a polymorphism of ApoE genotype. J. Cell. Mol. Med. *9*, 698–703. 10.1111/j.1582-4934.2005.tb00500.x.

17. Busch, R.M., Lineweaver, T.T., Naugle, R.I., Kim, K.H., Gong, Y., Tilelli, C.Q., Prayson, R.A., Bingaman, W., Najm, I.M., and Diaz-Arrastia, R. (2007). ApoE-epsilon4 is associated with reduced memory in long-standing intractable temporal lobe epilepsy. Neurology *68*, 409–414. 10.1212/01.wnl.0000253021.60887.db.

18. Gambardella, A., Aguglia, U., Chifari, R., Labate, A., Manna, I., Serra, P., Romeo, N., Sibilia, G., Lepiane, E., Russa, A.L., et al. (2005). ApoE epsilon4 allele and disease duration affect verbal learning in mild temporal lobe epilepsy. Epilepsia *46*, 110–117. 10.1111/j.0013-9580.2005.15804.x.

19. Vossel, K.A., Ranasinghe, K.G., Beagle, A.J., Mizuiri, D., Honma, S.M., Dowling, A.F., Darwish, S.M., Berlo, V.V., Barnes, D.E., Mantle, M., et al. (2016). Incidence and impact of subclinical epileptiform activity in Alzheimer's disease. Ann Neurol *80*, 858–870. 10.1002/ana.24794.

20. Vossel, K.A., Tartaglia, M.C., Nygaard, H.B., Zeman, A.Z., and Miller, B.L. (2017). Epileptic activity in Alzheimer's disease: causes and clinical relevance. Lancet Neurol *16*, 311–322. 10.1016/s1474-4422(17)30044-3.

21. Vossel, K.A., Beagle, A.J., Rabinovici, G.D., Shu, H., Lee, S.E., Naasan, G., Hegde, M., Cornes, S.B., Henry, M.L., Nelson, A.B., et al. (2013). Seizures and epileptiform activity in the early stages of Alzheimer disease. JAMA Neurol *70*, 1158–1166. 10.1001/jamaneurol.2013.136.

22. Brunetti, V., D'Atri, A., Marca, G.D., Vollono, C., Marra, C., Vita, M.G., Scarpelli, S., Gennaro, L.D., and Rossini, P.M. (2020). Subclinical epileptiform activity during sleep in Alzheimer's disease and mild cognitive impairment. Clin Neurophysiol *131*, 1011–1018. 10.1016/j.clinph.2020.02.015.

23. Lam, A.D., Sarkis, R.A., Pellerin, K.R., Jing, J., Dworetzky, B.A., Hoch, D.B., Jacobs, C.S., Lee, J.W., Weisholtz, D.S., Zepeda, R., et al. (2020). Association of epileptiform abnormalities and seizures in Alzheimer disease. Neurology *95*, e2259–e2270. 10.1212/wnl.0000000000010612.

24. Cretin, B., Sellal, F., Philippi, N., Bousiges, O., Bitonto, L.D., Martin-Hunyadi, C., and Blanc, F. (2016). Epileptic Prodromal Alzheimer's Disease, a Retrospective Study of 13 New Cases: Expanding the Spectrum of Alzheimer's Disease to an Epileptic Variant? J Alzheimers Dis *52*, 1125–1133. 10.3233/jad-150096.

25. DiFrancesco, J.C., Tremolizzo, L., Polonia, V., Giussani, G., Bianchi, E., Franchi, C., Nobili, A., Appollonio, I., Beghi, E., and Ferrarese, C. (2017). Adult-Onset Epilepsy in Presymptomatic Alzheimer's Disease: A Retrospective Study. Journal of Alzheimer's Disease *60*, 1267–1274. 10.3233/jad-170392.

26. Tombini, M., Assenza, G., Ricci, L., Lanzone, J., Boscarino, M., Vico, C., Magliozzi, A., and Lazzaro, V.D. (2021). Temporal Lobe Epilepsy and Alzheimer's Disease: From Preclinical to Clinical Evidence of a Strong Association. J Alzheimers Dis Rep *5*, 243–261. 10.3233/adr-200286.

27. Giorgi, F.S., Saccaro, L.F., Busceti, C.L., Biagioni, F., and Fornai, F. (2020). Epilepsy and Alzheimer's Disease: Potential mechanisms for an association. Brain Res. Bull. *160*, 107–120. 10.1016/j.brainresbull.2020.04.009.

28. Beghi, E., and Beghi, M. (2020). Epilepsy, antiepileptic drugs and dementia. Curr Opin Neurol *33*, 191–197. 10.1097/wco.0000000000000802.

29. Chen, H.-K., Ji, Z.-S., Dodson, S.E., Miranda, R.D., Rosenblum, C.I., Reynolds, I.J., Freedman, S.B., Weisgraber, K.H., Huang, Y., and Mahley, R.W. (2011). Apolipoprotein E4 domain interaction mediates detrimental effects on mitochondria and is a potential therapeutic target for Alzheimer disease. Journal of Biological Chemistry *286*, 5215–5221. 10.1074/jbc.m110.151084.

30. Huang, Y., and Mucke, L. (2012). Alzheimer mechanisms and therapeutic strategies. Cell *148*, 1204–1222. 10.1016/j.cell.2012.02.040.

31. Najm, R., Jones, E.A., and Huang, Y. (2019). Apolipoprotein E4, inhibitory network dysfunction, and Alzheimer's disease. Molecular Neurodegeneration *14*, 24. 10.1186/s13024-019-0324-6.

32. Andrews-Zwilling, Y., Bien-Ly, N., Xu, Q., Li, G., Bernardo, A., Yoon, S.Y., Zwilling, D., Yan, T.X., Chen, L., and Huang, Y. (2010). Apolipoprotein E4 causes age- and Tau-dependent impairment of GABAergic interneurons, leading to learning and memory deficits in mice. Journal of Neuroscience *30*, 13707–13717. 10.1523/jneurosci.4040-10.2010.

33. Leung, L., Andrews-Zwilling, Y., Yoon, S.Y., Jain, S., Ring, K., Dai, J., Wang, M.M., Tong, L., Walker, D., and Huang, Y. (2012). Apolipoprotein E4 causes age- and sex-dependent impairments of hilar GABAergic interneurons and learning and memory deficits in mice. PLoS ONE *7*, e53569. 10.1371/journal.pone.0053569.

34. Hunter, J.M., Cirrito, J.R., Restivo, J.L., Kinley, R.D., Sullivan, P.M., Holtzman, D.M., Koger, D., Delong, C., Lin, S., Zhao, L., et al. (2012). Emergence of a seizure phenotype in aged apolipoprotein epsilon 4 targeted replacement mice. Brain Res *1467*, 120–132. 10.1016/j.brainres.2012.05.048.

35. Lamoureux, L., Marottoli, F.M., Tseng, K.Y., and Tai, L.M. (2021). APOE4 Promotes Tonic-Clonic Seizures, an Effect Modified by Familial Alzheimer's Disease Mutations. Front. Cell Dev. Biol. *9*. 10.3389/fcell.2021.656521.

36. Nuriel, T., Angulo, S.L., Khan, U., Ashok, A., Chen, Q., Figueroa, H.Y., Emrani, S., Liu, L., Herman, M., Barrett, G., et al. (2017). Neuronal hyperactivity due to loss of inhibitory tone in APOE4 mice lacking Alzheimer's disease-like pathology. Nature Communications, 1–14. 10.1038/s41467-017-01444-0.

37. Tong, L.M., Yoon, S.Y., Andrews-Zwilling, Y., Yang, A., Lin, V., Lei, H., and Huang, Y. (2016). Enhancing GABA Signaling during Middle Adulthood Prevents Age-Dependent GABAergic Interneuron Decline and Learning and Memory Deficits in ApoE4 Mice. Journal of Neuroscience *36*, 2316–2322. 10.1523/jneurosci.3815-15.2016.

38. Knoferle, J., Yoon, S.Y., Walker, D., Leung, L., Gillespie, A.K., Tong, L.M., Bien-Ly, N., and Huang, Y. (2014). Apolipoprotein E4 produced in GABAergic interneurons causes learning and memory deficits in mice. Journal of Neuroscience *34*, 14069–14078. 10.1523/jneurosci.2281-14.2014.

39. Taubes, A., Nova, P., Zalocusky, K.A., Kosti, I., Bicak, M., Zilberter, M., Hao, Y., Yoon, S.Y., Oskotsky, T., Pineda, S., et al. (2021). Experimental and real-world evidence supporting the computational repurposing of bumetanide for APOE4-related Alzheimer's disease. Nature Aging *1*, 932–947. 10.1038/s43587-021-00122-7.

40. Zalocusky, K.A., Najm, R., Taubes, A.L., Hao, Y., Yoon, S.Y., Koutsodendris, N., Nelson, M.R., Rao, A., Bennett, D.A., Bant, J., et al. (2021). Neuronal ApoE upregulates MHC-I expression to drive selective neurodegeneration in Alzheimer's disease. Nat Neurosci *24*, 786–798. 10.1038/s41593-021-00851-3.

41. Koutsodendris, N., Blumenfeld, J., Agrawal, A., Traglia, M., Grone, B., Zilberter, M., Yip, O., Rao, A., Nelson, M.R., Hao, Y., et al. (2023). Neuronal APOE4 removal protects against tau-mediated gliosis, neurodegeneration and myelin deficits. Nature Aging *3*, 275–296. 10.1038/s43587-023-00368-3.

42. Koch, C. (2004). Biophysics of Computation (Oxford University Press).

43. Torres-Torrelo, J., Torres, B., and Carrascal, L. (2014). Modulation of the input-output function by GABAA receptor-mediated currents in rat oculomotor nucleus motoneurons. The Journal of Physiology *592*, 5047–5064. 10.1113/jphysiol.2014.276576.

44. Sun, Q., Jiang, Y.-Q., and Lu, M.C. (2020). Topographic heterogeneity of intrinsic excitability in mouse hippocampal CA3 pyramidal neurons. J Neurophysiol *124*, 1270–1284. 10.1152/jn.00147.2020.

45. Ghatak, S., Dolatabadi, N., Trudler, D., Zhang, X., Wu, Y., Mohata, M., Ambasudhan, R., Talantova, M., and Lipton, S.A. (2019). Mechanisms of hyperexcitability in Alzheimer's disease hiPSC-derived neurons and cerebral organoids vs isogenic controls. Elife *8*. 10.7554/elife.50333.

46. Šišková, Z., Justus, D., Kaneko, H., Friedrichs, D., Henneberg, N., Beutel, T., Pitsch, J., Schoch, S., Becker, A., Kammer, H. von der, et al. (2014). Dendritic structural degeneration is functionally linked to cellular hyperexcitability in a mouse model of Alzheimer's disease. Neuron *84*, 1023–1033. 10.1016/j.neuron.2014.10.024.

47. Nenov, M.N., Tempia, F., Denner, L., Dineley, K.T., and Laezza, F. (2015). Impaired firing properties of dentate granule neurons in an Alzheimer's disease animal model are rescued by PPARγ agonism. J Neurophysiol *113*, 1712–1726. 10.1152/jn.00419.2014.

48. Xu, Q., Walker, D., Bernardo, A., Brodbeck, J., Balestra, M.E., and Huang, Y. (2008). Intron-3 retention/splicing controls neuronal expression of apolipoprotein E in the CNS. Journal of Neuroscience *28*, 1452–1459. 10.1523/jneurosci.3253-07.2008.

49. Jain, S., Yoon, S.Y., Leung, L., Knoferle, J., and Huang, Y. (2013). Cellular source-specific effects of apolipoprotein (apo) E4 on dendrite arborization and dendritic spine development. PLoS ONE *8*, e59478. 10.1371/journal.pone.0059478.

50. Duigou, C.L., Simonnet, J., Teleñczuk, M.T., Fricker, D., and Miles, R. (2014). Recurrent synapses and circuits in the CA3 region of the hippocampus: an associative network. Front Cell Neurosci *7*, 262. 10.3389/fncel.2013.00262.

51. Gilbert, L.A., Larson, M.H., Morsut, L., Liu, Z., Brar, G.A., Torres, S.E., Stern-Ginossar, N., Brandman, O., Whitehead, E.H., Doudna, J.A., et al. (2013). CRISPR-mediated modular RNA-guided regulation of transcription in eukaryotes. Cell *154*, 442–451. 10.1016/j.cell.2013.06.044.

52. Kuroda, S., and Tanizawa, K. (1999). Involvement of epidermal growth factor-like domain of NELL proteins in the novel protein-protein interaction with protein kinase C. Biochem. Biophys. Res. Commun. *265*, 752–757. 10.1006/bbrc.1999.1753.

53. Ha, C.M., Kim, D.H., Lee, T.H., Kim, H.R., Choi, J., Kim, Y., Kang, D., Park, J.W., Ojeda, S.R., Jeong, J.K., et al. (2022). Transcriptional Regulatory Role of NELL2 in Preproenkephalin Gene Expression. Mol Cells *45*, 537–549. 10.14348/molcells.2022.2051.

54. Aihara, K., Kuroda, S., Kanayama, N., Matsuyama, S., Tanizawa, K., and Horie, M. (2003). A neuron-specific EGF family protein, NELL2, promotes survival of neurons through mitogen-activated protein kinases. Brain Res. Mol. Brain Res. *116*, 86–93. 10.1016/s0169-328x(03)00256-0.

55. Nelson, B.R., Claes, K., Todd, V., Chaverra, M., and Lefcort, F. (2004). NELL2 promotes motor and sensory neuron differentiation and stimulates mitogenesis in DRG in vivo. Dev Biol *270*, 322–335. 10.1016/j.ydbio.2004.03.004.

56. Jeong, J.K., Kim, H.R., Hwang, S.M., Park, J.W., and Lee, B.J. (2008). Region- and neuronal phenotype-specific expression of NELL2 in the adult rat brain. Mol Cells *26*, 186–192.

57. Lesca, G., Rudolf, G., Labalme, A., Hirsch, E., Arzimanoglou, A., Genton, P., Motte, J., Martin, A. de S., Valenti, M.-P., Boulay, C., et al. (2012). Epileptic encephalopathies of the Landau-Kleffner and continuous spike and waves during slow-wave sleep types: genomic dissection makes the link with autism. Epilepsia *53*, 1526–1538. 10.1111/j.1528-1167.2012.03559.x.

58. Filippini, N., MacIntosh, B.J., Hough, M.G., Goodwin, G.M., Frisoni, G.B., Smith, S.M., Matthews, P.M., Beckmann, C.F., and Mackay, C.E. (2009). Distinct patterns of brain activity in young carriers of the APOE-ε4 allele. Proc Natl Acad Sci USA *106*, 7209–7214. 10.1073/pnas.0811879106.

59. Dennis, N.A., Browndyke, J.N., Stokes, J., Need, A., Burke, J.R., Welsh-Bohmer, K.A., and Cabeza, R. (2010). Temporal lobe functional activity and connectivity in young adult APOE varepsilon4 carriers. Alzheimers Dement *6*, 303–311. 10.1016/j.jalz.2009.07.003.

60. Minkeviciene, R., Rheims, S., Dobszay, M.B., Zilberter, M., Hartikainen, J., Fülöp, L., Penke, B., Zilberter, Y., Harkany, T., Pitkänen, A., et al. (2009). Amyloid beta-induced neuronal hyperexcitability triggers progressive epilepsy. Journal of Neuroscience *29*, 3453–3462. 10.1523/jneurosci.5215-08.2009.

61. Zilberter, M., Ivanov, A., Ziyatdinova, S., Mukhtarov, M., Malkov, A., Alpár, A., Tortoriello, G., Botting, C.H., Fülöp, L., Osypov, A.A., et al. (2013). Dietary energy substrates reverse early neuronal hyperactivity in a mouse model of Alzheimer's disease. Journal of Neurochemistry *125*, 157–171. 10.1111/jnc.12127.

62. Palop, J.J., Chin, J., Roberson, E.D., Wang, J., Thwin, M.T., Bien-Ly, N., Yoo, J., Ho, K.O., Yu, G.-Q., Kreitzer, A., et al. (2007). Aberrant excitatory neuronal activity and compensatory remodeling of inhibitory hippocampal circuits in mouse models of Alzheimer's disease. Neuron *55*, 697–711. 10.1016/j.neuron.2007.07.025.

63. Popova, I., Malkov, A., Ivanov, A.I., Samokhina, E., Buldakova, S., Gubkina, O., Osypov, A., Muhammadiev, R.S., Zilberter, T., Molchanov, M., et al. (2017). Metabolic correction by pyruvate halts acquired epilepsy in multiple rodent models. Neurobiol Dis *106*, 244–254. 10.1016/j.nbd.2017.07.012.

64. Busche, M.A., Chen, X., Henning, H.A., Reichwald, J., Staufenbiel, M., Sakmann, B., and Konnerth, A. (2012). Critical role of soluble amyloid-β for early hippocampal hyperactivity in a mouse model of Alzheimer's disease. Proceedings of the National Academy of Sciences *109*, 8740–8745. 10.1073/pnas.1206171109.

65. Verret, L., Mann, E.O., Hang, G.B., Barth, A.M.I., Cobos, I., Ho, K., Devidze, N., Masliah, E., Kreitzer, A.C., Mody, I., et al. (2012). Inhibitory interneuron deficit links altered network activity and cognitive dysfunction in Alzheimer model. Cell *149*, 708–721. 10.1016/j.cell.2012.02.046.

66. Kellner, V., Menkes-Caspi, N., Beker, S., and Stern, E.A. (2014). Amyloid-β alters ongoing neuronal activity and excitability in the frontal cortex. Neurobiology of Aging *35*, 1982–1991. 10.1016/j.neurobiolaging.2014.04.001.

67. Scala, F., Fusco, S., Ripoli, C., Piacentini, R., Puma, D.D.L., Spinelli, M., Laezza, F., Grassi, C., and D'Ascenzo, M. (2015). Intraneuronal Aβ accumulation induces hippocampal neuron hyperexcitability through A-type K(+) current inhibition mediated by activation of caspases and GSK-3. Neurobiology of Aging *36*, 886–900. 10.1016/j.neurobiolaging.2014.10.034.

68. Gentet, L.J., Stuart, G.J., and Clements, J.D. (2000). Direct measurement of specific membrane capacitance in neurons. Biophysical Journal *79*, 314–320. 10.1016/s0006-3495(00)76293-x.

69. Aboud, O., Mrak, R.E., Boop, F., and Griffin, S.T. (2012). Apolipoprotein epsilon 3 alleles are associated with indicators of neuronal resilience. BMC Med *10*, 35–10. 10.1186/1741-7015-10-35.

70. Buttini, M., Masliah, E., Yu, G.-Q., Palop, J.J., Chang, S., Bernardo, A., Lin, C., Wyss-Coray, T., Huang, Y., and Mucke, L. (2010). Cellular source of apolipoprotein E4 determines neuronal susceptibility to excitotoxic injury in transgenic mice. Am. J. Pathol. *177*, 563–569. 10.2353/ajpath.2010.090973.

71. Xu, Q. (2006). Profile and Regulation of Apolipoprotein E (ApoE) Expression in the CNS in Mice with Targeting of Green Fluorescent Protein Gene to the ApoE Locus. J Neurosci *26*, 4985–4994. 10.1523/jneurosci.5476-05.2006.

72. Huang, Y. (2010). Abeta-independent roles of apolipoprotein E4 in the pathogenesis of Alzheimer's disease. Trends Mol Med *16*, 287–294. 10.1016/j.molmed.2010.04.004.

73. Chang, S., Ma, T. ran, Miranda, R.D., Balestra, M.E., Mahley, R.W., and Huang, Y. (2005). Lipid- and receptor-binding regions of apolipoprotein E4 fragments act in concert to cause mitochondrial dysfunction and neurotoxicity. Proc Natl Acad Sci USA *102*, 18694–18699. 10.1073/pnas.0508254102.

74. Brecht, W.J., Harris, F.M., Chang, S., Tesseur, I., Yu, G.-Q., Xu, Q., Fish, J.D., Wyss-Coray, T., Buttini, M., Mucke, L., et al. (2004). Neuron-specific apolipoprotein e4 proteolysis is associated with increased tau phosphorylation in brains of transgenic mice. Journal of Neuroscience *24*, 2527–2534. 10.1523/jneurosci.4315-03.2004.

75. Robitsek, J., Ratner, M.H., Stewart, T., Eichenbaum, H., and Farb, D.H. (2015). Combined administration of levetiracetam and valproic acid attenuates age-related hyperactivity of CA3 place cells, reduces place field area, and increases spatial information content in aged rat hippocampus. Hippocampus *25*, 1541–1555. 10.1002/hipo.22474.

76. Haberman, R.P., Koh, M.T., and Gallagher, M. (2017). Heightened cortical excitability in aged rodents with memory impairment. Neurobiol. Aging *54*, 144–151. 10.1016/j.neurobiolaging.2016.12.021.

77. Lee, H., Wang, Z., Zeger, S.L., Gallagher, M., and Knierim, J.J. (2021). Heterogeneity of Age-Related Neural Hyperactivity along the CA3 Transverse Axis. Journal of Neuroscience *41*, 663–673. 10.1523/jneurosci.2405-20.2020.

78. Koh, M.T., Branch, A., Haberman, R., and Gallagher, M. (2020). Significance of inhibitory recruitment in aging with preserved cognition: limiting gamma-aminobutyric acid type A α5 function produces memory impairment. Neurobiol. Aging *91*, 1–4. 10.1016/j.neurobiolaging.2020.02.019.

79. Thomé, A., Gray, D.T., Erickson, C.A., Lipa, P., and Barnes, C.A. (2016). Memory impairment in aged primates is associated with region-specific network dysfunction. Mol. Psychiatry *21*, 1257–1262. 10.1038/mp.2015.160.

80. Chang, C.-W., Shao, E., and Mucke, L. (2021). Tau: Enabler of diverse brain disorders and target of rapidly evolving therapeutic strategies. Science *371*. 10.1126/science.abb8255.

81. Tracy, T.E., and Gan, L. (2018). Tau-mediated synaptic and neuronal dysfunction in neurodegenerative disease. Curr. Opin. Neurobiol. *51*, 134–138. 10.1016/j.conb.2018.04.027.

82. Tesseur, I., Dorpe, J.V., Spittaels, K., Haute, C.V. den, Moechars, D., and Leuven, F.V. (2000). Expression of human apolipoprotein E4 in neurons causes hyperphosphorylation of protein tau in the brains of transgenic mice. Am. J. Pathol. *156*, 951–964. 10.1016/s0002-9440(10)64963-2.

83. Zheng, W.-H., Bastianetto, S., Mennicken, F., Ma, W., and Kar, S. (2002). Amyloid beta peptide induces tau phosphorylation and loss of cholinergic neurons in rat primary septal cultures. Neuroscience *115*, 201–211. 10.1016/s0306-4522(02)00404-9.

84. Lloret, A., Badia, M.-C., Giraldo, E., Ermak, G., Alonso, M.-D., Pallardó, F.V., Davies, K.J.A., and Viña, J. (2011). Amyloid-β toxicity and tau hyperphosphorylation are linked via RCAN1 in Alzheimer's disease. J Alzheimers Dis *27*, 701–709. 10.3233/jad-2011-110890.

85. Tokutake, T., Kasuga, K., Yajima, R., Sekine, Y., Tezuka, T., Nishizawa, M., and Ikeuchi, T. (2012). Hyperphosphorylation of Tau Induced by Naturally Secreted Amyloid-beta at Nanomolar Concentrations Is Modulated by Insulin-dependent Akt-GSK3Î² Signaling Pathway*. J Biol Chem *287*, 35222–35233. 10.1074/jbc.m112.348300.

86. Stancu, I.-C., Vasconcelos, B., Terwel, D., and Dewachter, I. (2014). Models of β-amyloid induced Tau-pathology: the long and "folded" road to understand the mechanism. Molecular Neurodegeneration *9*, 51–14. 10.1186/1750-1326-9-51.

87. Roberson, E.D., Scearce-Levie, K., Palop, J.J., Yan, F., Cheng, I.H., Wu, T., Gerstein, H., Yu, G.-Q., and Mucke, L. (2007). Reducing endogenous tau ameliorates amyloid beta-induced deficits in an Alzheimer's disease mouse model. Science *316*, 750–754. 10.1126/science.1141736.

88. Hall, A.M., Throesch, B.T., Buckingham, S.C., Markwardt, S.J., Peng, Y., Wang, Q., Hoffman, D.A., and Roberson, E.D. (2015). Tau-dependent kv4.2 depletion and dendritic hyperexcitability in a mouse model of Alzheimer's disease. Journal of Neuroscience *35*, 6221–6230. 10.1523/jneurosci.2552-14.2015.

89. Chen, H., Herndon, M.E., and Lawler, J. (2000). The cell biology of thrombospondin-1. Matrix Biol *19*, 597–614. 10.1016/s0945-053x(00)00107-4.

90. Hwang, E.M., Kim, D.-G., Lee, B.J., Choi, J., Kim, E., Park, N., Kang, D., Han, J., Choi, W.S., Hong, S.-G., et al. (2007). Alternative splicing generates a novel non-secretable cytosolic isoform of NELL2. Biochem. Biophys. Res. Commun. *353*, 805–811. 10.1016/j.bbrc.2006.12.115.

91. Lopes, F.B.T.P., Schlatzer, D., Wang, R., Li, X., Feng, E., Koyutürk, M., Qi, X., and Chance, M.R. (2022). Temporal and Sex-Linked Protein Expression Dynamics in a Familial Model of Alzheimer's Disease. Mol Cell Proteomics *21*, 100280. 10.1016/j.mcpro.2022.100280.

92. Puri, S., Hu, J., Sun, Z., Lin, M., Stein, T.D., Farrer, L.A., Wolozin, B., and Zhang, X. (2023). Identification of circRNAs linked to Alzheimer's disease and related dementias. Alzheimers Dement. 10.1002/alz.12960.

93. Sullivan, P.M., Mace, B.E., Maeda, N., and Schmechel, D.E. (2004). Marked regional differences of brain human apolipoprotein E expression in targeted replacement mice. Neuroscience *124*, 725–733. 10.1016/j.neuroscience.2003.10.011.

94. Bien-Ly, N., Gillespie, A.K., Walker, D., Yoon, S.Y., and Huang, Y. (2012). Reducing human apolipoprotein E levels attenuates age-dependent Aβ accumulation in mutant human amyloid precursor protein transgenic mice. Journal of Neuroscience *32*, 4803–4811. 10.1523/jneurosci.0033-12.2012.

95. Bajenaru, M.L., Zhu, Y., Hedrick, N.M., Donahoe, J., Parada, L.F., and Gutmann, D.H. (2002). Astrocyte-specific inactivation of the neurofibromatosis 1 gene (NF1) is insufficient for astrocytoma formation. Mol Cell Biol *22*, 5100–5113. 10.1128/mcb.22.14.5100-5113.2002.

96. Uhlmann, E.J., Wong, M., Baldwin, R.L., Bajenaru, M.L., Onda, H., Kwiatkowski, D.J., Yamada, K., and Gutmann, D.H. (2002). Astrocyte-specific TSC1 conditional knockout mice exhibit abnormal neuronal organization and seizures. Ann Neurol *52*, 285–296. 10.1002/ana.10283.

97. Zhu, Y., Romero, M.I., Ghosh, P., Ye, Z., Charnay, P., Rushing, E.J., Marth, J.D., and Parada, L.F. (2001). Ablation of NF1 function in neurons induces abnormal development of cerebral cortex and reactive gliosis in the brain. Genes Dev *15*, 859–876. 10.1101/gad.862101.

98. Butler, A., Hoffman, P., Smibert, P., Papalexi, E., and Satija, R. (2018). Integrating single-cell transcriptomic data across different conditions, technologies, and species. Nat Biotechnol *36*, 411–420. 10.1038/nbt.4096.

99. Stuart, T., Butler, A., Hoffman, P., Hafemeister, C., Papalexi, E., Mauck, W.M., Hao, Y., Stoeckius, M., Smibert, P., and Satija, R. (2019). Comprehensive Integration of Single-Cell Data. Cell *177*, 1888-1902.e21. 10.1016/j.cell.2019.05.031.

100. Zhang, Y., Chen, K., Sloan, S.A., Bennett, M.L., Scholze, A.R., O'Keeffe, S., Phatnani, H.P., Guarnieri, P., Caneda, C., Ruderisch, N., et al. (2014). An RNA-Sequencing Transcriptome and Splicing Database of Glia, Neurons, and Vascular Cells of the Cerebral Cortex. J Neurosci *34*, 11929–11947. 10.1523/jneurosci.1860-14.2014.

101. Cembrowski, M.S., Wang, L., Sugino, K., Shields, B.C., and Spruston, N. (2016). Hipposeq: a comprehensive RNA-seq database of gene expression in hippocampal principal neurons. Elife *5*, e14997. 10.7554/elife.14997.

102. Saunders, A., Macosko, E.Z., Wysoker, A., Goldman, M., Krienen, F.M., Rivera, H. de, Bien, E., Baum, M., Bortolin, L., Wang, S., et al. (2018). Molecular Diversity and Specializations among the Cells of the Adult Mouse Brain. Cell *174*, 1015-1030.e16. 10.1016/j.cell.2018.07.028.

103. Lein, E.S., Hawrylycz, M.J., Ao, N., Ayres, M., Bensinger, A., Bernard, A., Boe, A.F., Boguski, M.S., Brockway, K.S., Byrnes, E.J., et al. (2007). Genome-wide atlas of gene expression in the adult mouse brain. Nature *445*, 168–176. 10.1038/nature05453.

104. Thakore, P.I., D'Ippolito, A.M., Song, L., Safi, A., Shivakumar, N.K., Kabadi, A.M., Reddy, T.E., Crawford, G.E., and Gersbach, C.A. (2015). Highly specific epigenome editing by CRISPR-Cas9 repressors for silencing of distal regulatory elements. Nat. Methods *12*, 1143–1149. 10.1038/nmeth.3630.

105. Ernst, J., and Kellis, M. (2015). Large-scale imputation of epigenomic datasets for systematic annotation of diverse human tissues. Nat Biotechnol *33*, 364–376. 10.1038/nbt.3157.

106. Hartigan, J.A., and Wong, M.A. (1979). Algorithm AS 136: A K-Means Clustering Algorithm. Journal of the Royal Statistical Society. Series C (Applied Statistics) *28*, 100–108.

107. Pedregosa, F., Varoquaux, G., Gramfort, A., Michel, V., Thirion, B., Grisel, O., Blondel, M., Müller, A., Nothman, J., Louppe, G., et al. (2011). Scikit-learn: Machine Learning in Python. JLMR, 2825–2830.

108. Seabold, S., and Perktold, J. (2010). Statsmodels: Econometric and Statistical Modeling with Python. Proc. 9th Python Sci. Conf., 92–96. 10.25080/majora-92bf1922-011.

SUPPLEMENTARY FIGURES

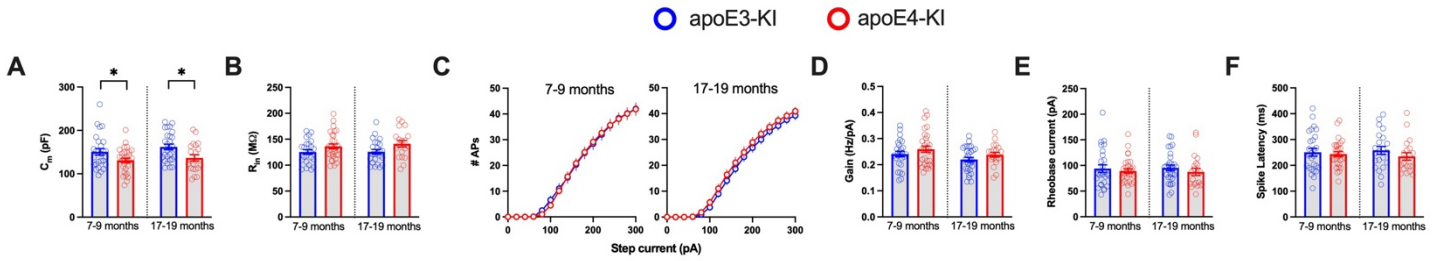

Supplementary Figure 1. Lack of apoE4-driven hyperexcitability phenotype in hippocampal CA1 Pyramidal cells (PCs).

Neurons were recorded from apoE3-KI (blue) and apoE4-KI (red) mice at ages of 7–9 months and 17–19 months.

(A) Cell capacitance (C_m) values.

(B) Input resistance (R_{in}) values.

(C) Input current – firing rate relationship (I-F Curve), the average number of spikes elicited by 1sec epochs of increasing depolarizing current injections.

(D) Firing gain values quantified as the linear slope of the I-F curve.

(E) Rheobase values, the minimum depolarizing current required to elicit an action potential;

(F) Spike Latency, the delay to first spike in response to an 800pA, 1sec ramped depolarizing current injection.

*$p<0.05$, unpaired two-tailed t-test or Mann-Whitney test. N = 4 mice each for 7–9 month-old apoE3-KI and apoE4-KI mice and 4-6 mice for 17–19 month-old apoE3-KI and apoE4-KI mice. See also Supplementary Table 1.

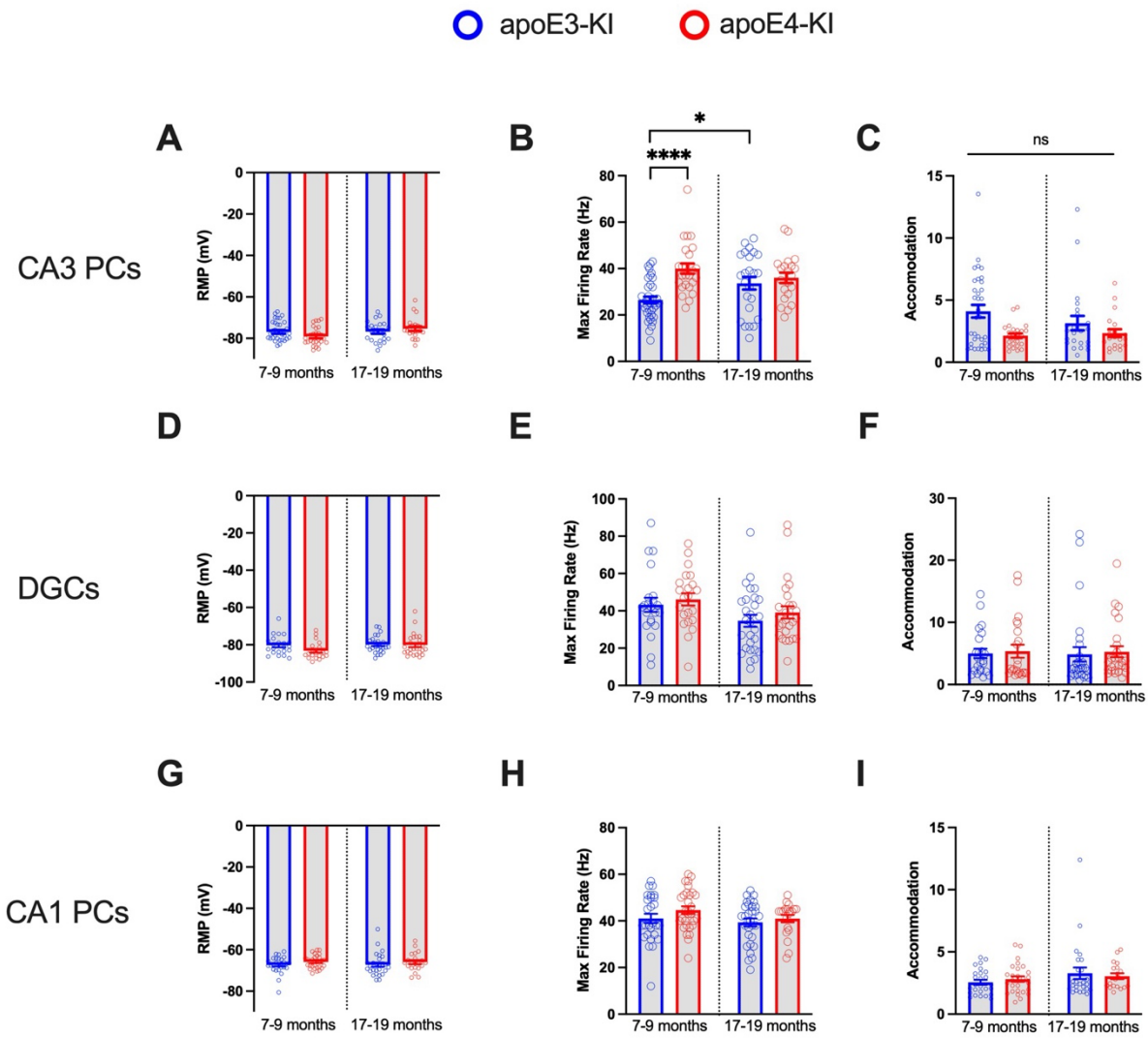

Supplementary Figure 2. Secondary intrinsic excitability parameters in hippocampal excitatory neurons. Parameters recorded in CA3 and CA1 PCs as well as DGCs from apoE3-KI (blue) and apoE4-KI (red) mice at ages of 7–9 months and 17–19 months are shown.

(A,D,G) Resting membrane potential (RMP) values.

(B,E,H) Maximal firing rate values.

(C,F,I) Firing accommodation values

*p<0.05, ****p<0.0001, unpaired two-tailed t-test or Mann-Whitney test. See also Supplementary Table 1.

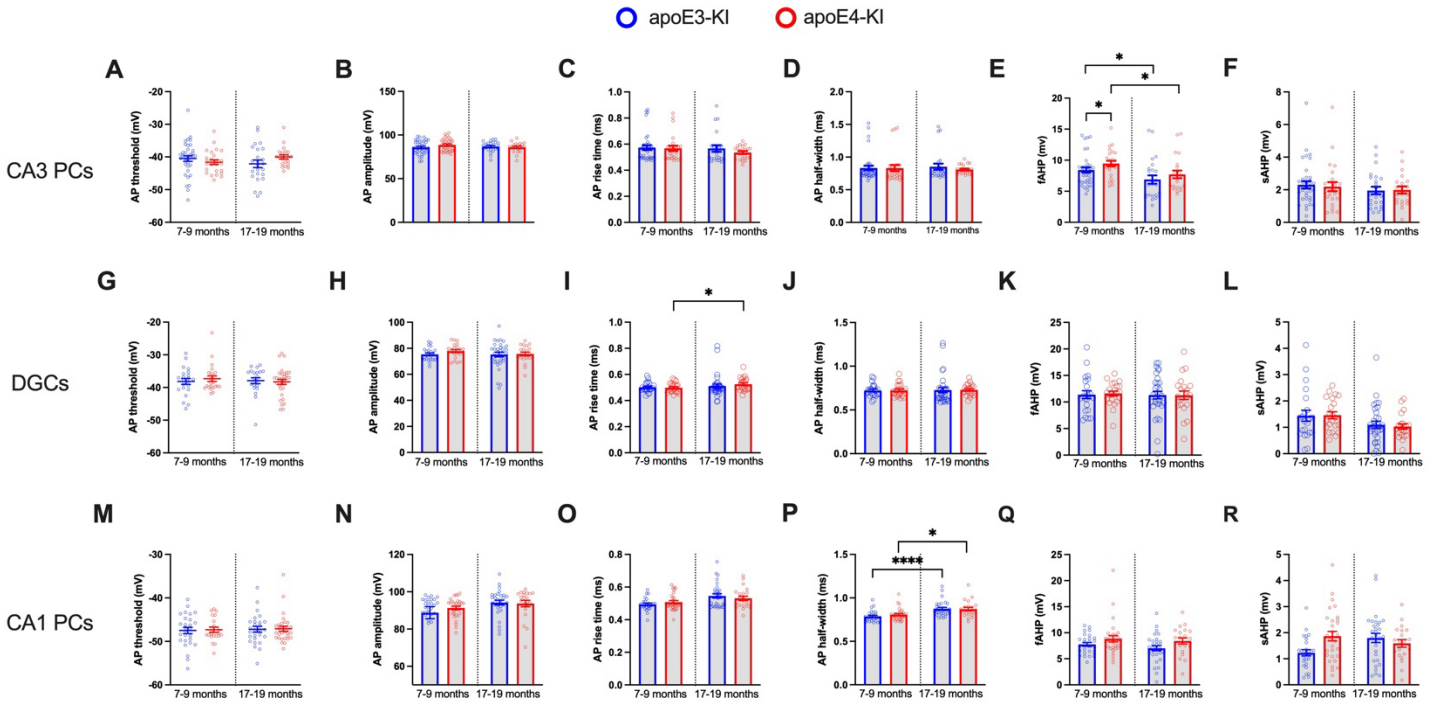

Supplementary Figure 3. Action potential-related excitability parameters in hippocampal excitatory neurons from apoE3-KI and apoE4-KI mice at 7–9 and 17–19 months of age. Shown are action potential (AP) waveform parameters:

(A,G,M) AP threshold potential.

(B,H,N) AP amplitude.

(C,I,O) AP rise time.

(D,J,P) AP half-width.

(E,K,Q) fast afterhyperpolarization (fAHP).

(F,L,R) slow afterhyperpolarization (sAHP).

*p<0.05, ****p<0.0001, unpaired two-tailed t-test or Mann-Whitney test. See also Supplementary Table 1.

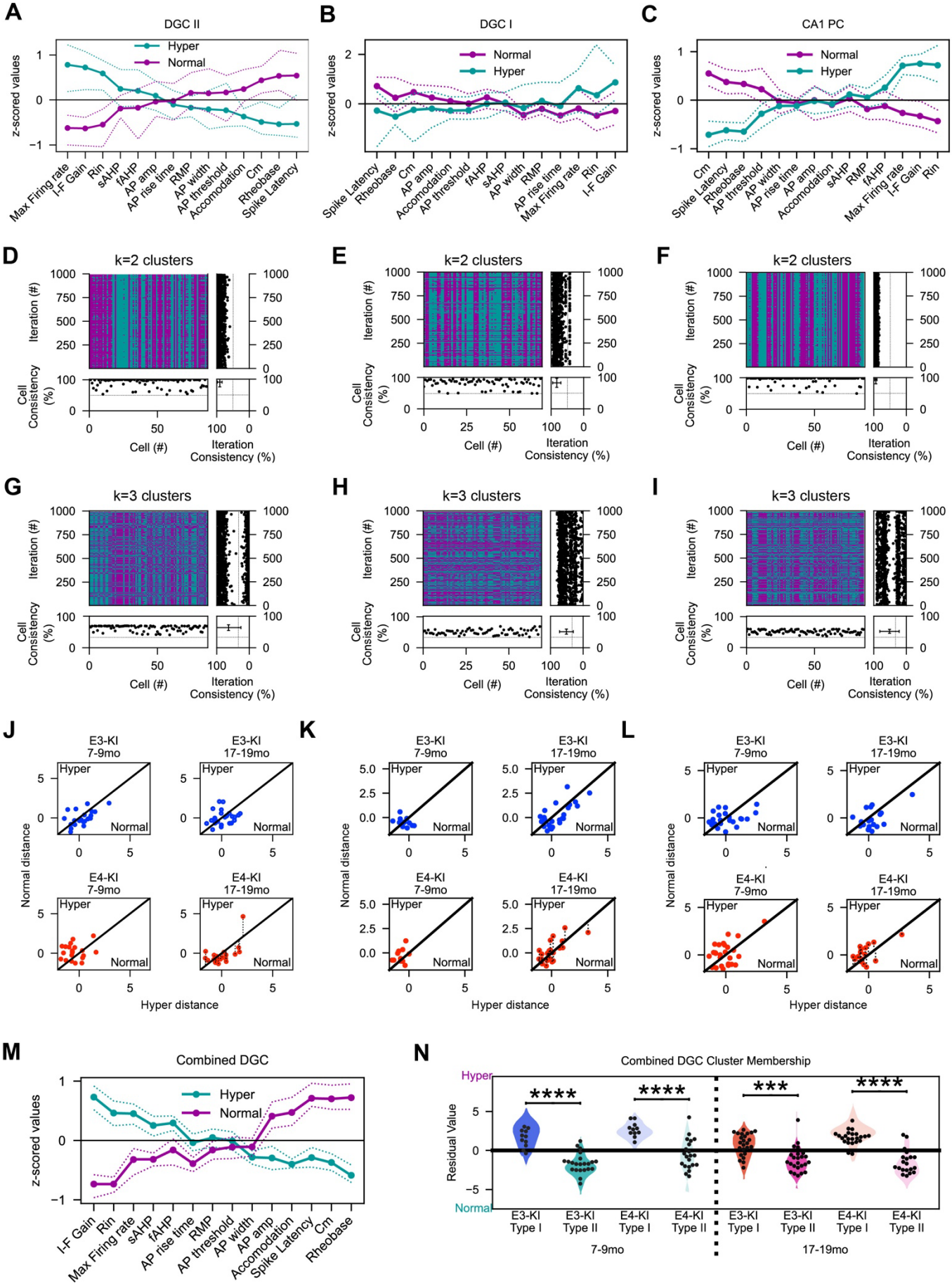
A
DGC II
Hyper
Normal
z-scored values
Max Firing rate
I-F Gain
Rin
sAHP
fAHP
AP amp
AP rise time
RMP
AP width
AP threshold
Accomodation
Cm
Rheobase
Spike Latency
B
DGC I
Normal
Hyper
C
CA1 PC
D
k=2 clusters
E
F
G
k=3 clusters
H
I
Iteration (#)
Cell Consistency (%)
Cell (#)
Iteration Consistency (%)
J
E3-KI 7-9mo
E3-KI 17-19mo
E4-KI 7-9mo
E4-KI 17-19mo
Normal distance
Hyper distance
K
L
M
Combined DGC
N
Combined DGC Cluster Membership
Residual Value
****
***
E3-KI Type I
E3-KI Type II
E4-KI Type I
E4-KI Type II
7-9mo
17-19mo

Supplementary Figure 4. Cluster analysis of DGC I, DGC II, and CA1 PC cells.

(*A–C) Centroids determined by k-means clustering into two clusters for DGCI, DGC II, and CA1 PCs respectively. Dashed lines indicate 99%CI determined from cross validation iterations.

(D–F) Cross validation analysis for each cell type with k=2 clusters. For each, heat map shows individual cell classification across each iteration. Upper Right) panel displays the probability of each iteration matching the classification of the full dataset. Bottom Left) panel displays the probability of a cell maintaining is classification identity across iterations. Lower Right) mean probabilities across iterations. Dashed lines indicate chance probability (50%).

(G–I) Same as in D–E but for 3 clusters, where chance indicators are at 33.3%.

(**J–L)** Scatter plot indicating the comparative distance from centroid for each cell binned by age genotype and cell type. Unity line represents the decision line between each hyperexcitable and normal.

(M) Centroids resulting from clustering with combined DGC types.

(N) Cluster distance residuals for DGC I & II grouped by age and genotype.

Significant differences were determined with a two-way ANOVA and Tukey post-hoc test. ***$p<0.001$, ****$p<0.0001$.

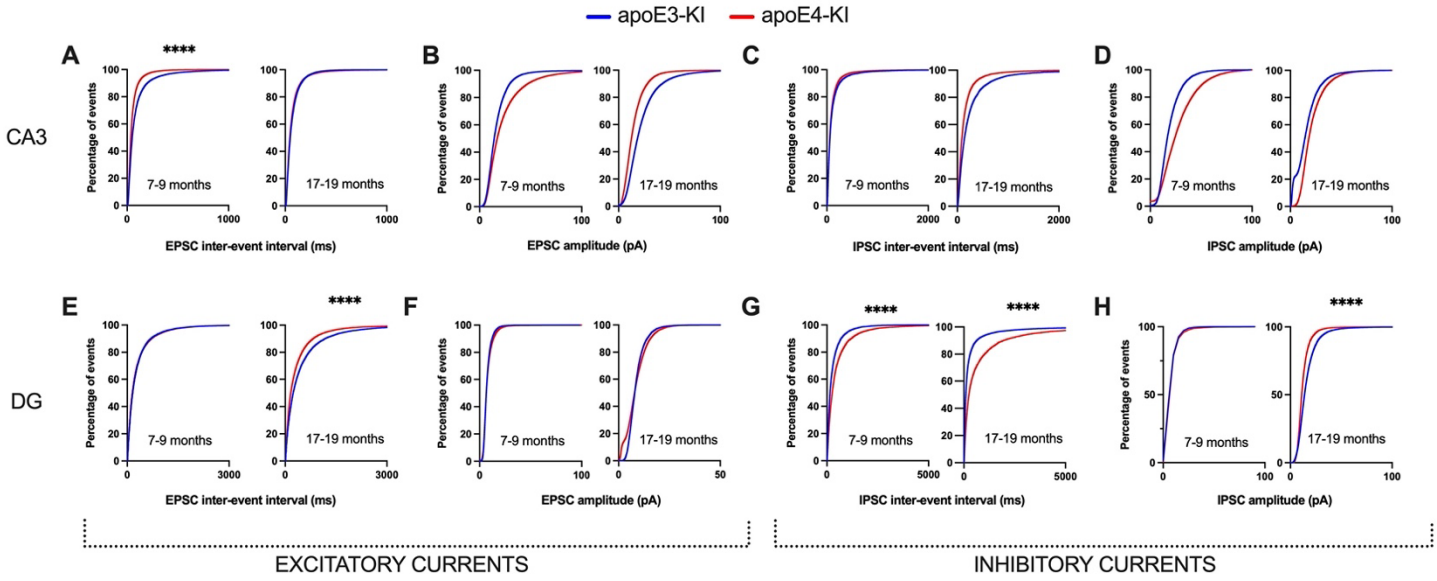

Supplementary Figure 5. Cumulative distributions for inter-event intervals and amplitudes of all synaptic events shown in Figure 6. First 1000 events in each recording were used for the analysis.

Significant differences were determined with Kolmogorov-Smirnov test. ****p<0.0001.

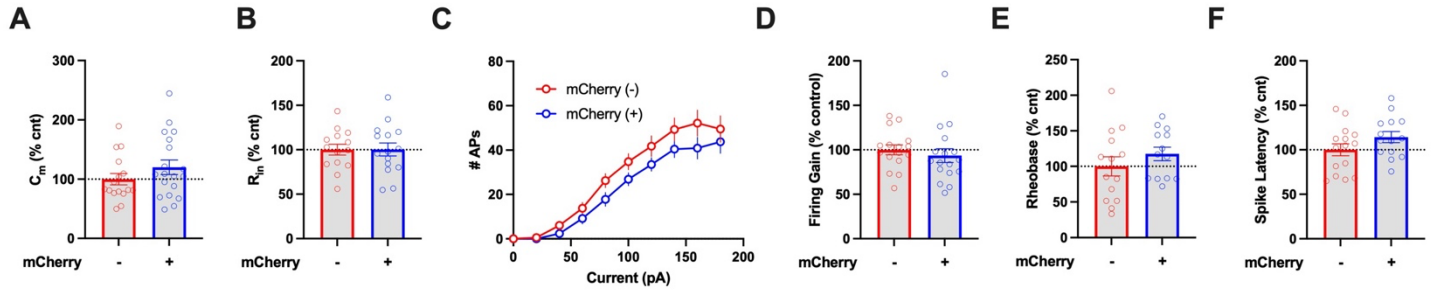

Supplementary Figure 6. Lack of Mdga2 CRISPRi effects on neuronal morpho-electric parameters in 7 month old apoE4-KI mice. Shown are parameters recorded in both mCherry+ and neighboring mCherry- DGCs.

(**A)** Membrane capacitance (C_m) values for mCherry- and mCherry+ cells, normalized to mCherry- average for each slice**.**

(B) Input resistance (R_{in}) values for mCherry- and mCherry+ cells, normalized to mCherry- average for each slice.

(C) Input current – firing rate relationships (I-F Curves), the average number of spikes elicited by incremental depolarizing current injections.

(D) Firing gain values, quantified as the linear slope of the I-F curve, normalized to mCherry- average for each slice.

(E) Rheobase values normalized to mCherry- average for each slice.

(F) Spike latency values normalized to mCherry- average for each slice.

All comparisons did not reach statistical significance with unpaired student t-test. See also Supplementary Table 4.

SUPPLEMENTARY TABLES

Supplementary Table 1. Detailed information on all neuronal parameters from apoE4-KI mice presented in Figures 1, 2, and S1–3.

Cell type		Parameter	Figure	MLR Test FDR Corrected	apoE3-KI 7-9 months Mean	SEM	n	N	17-19 months Mean	SEM	n	N	% vs. 7mo	p vs. 7mo	apoE4-KI 7-9 months Mean	SEM	n	N	% vs. apoE3	p vs. apoE3	17-19 months Mean	SEM	n	N	% vs. apoE3	p vs. apoE3	% vs. 7mo	p vs. 7mo
CA3 PCs	1	Cell capacitance (pF)	1A	0.0002	207.1	6.96	37	8	183.7	9.408	24	6	88.7	0.0459	169.6	6.35	25	7	81.9	0.0004	159.9	8.141	21	4	87.0	0.0661	94.3	0.345
	2	Input Resistance (Mohm)	1B	0.01071	260.9	11.6	37	8	309	18.5	21	6	118.4	0.0242	354.4	19.12	25	7	135.8	<0.0000	314.5	14.68	21	4	101.8	0.8161	88.7	0.116
	3	Firing gain (Hz/pA)	1D	0.00011	0.048	0.003	37	8	0.067	0.0048	24	6	139.8	0.0004	0.08	0.004	25	7	167.1	<0.0001	0.076	0.005	21	4	113.6	0.1899	95.1	0.52
	4	Rheobase (pA)	1E	0.01079	160.5	9.409	37	8	106.3	12.78	24	6	66.2	0.0004	96.08	9.882	25	7	59.9	<0.0001	105.3	9.916	21	4	99.1	0.8245	109.6	0.475
	5	Spike latency (ms)	1F	0.14562	241.3	8.676	36	8	201.1	14.94	22	6	83.3	0.015	204.5	11.56	25	7	84.7	0.0119	210.9	12.33	21	4	104.9	0.617	103.1	0.707
	6	Resting membrane potential (mV)	S2A	0.25684	-76.9	0.884	35	8	-76.7	0.9854	24	6	99.8	0.9201	-79.1	0.916	25	7	102.8	0.1001	-75.3	1.127	21	4	98.1	0.5614	95.3	0.012
	7	Max firing rate (Hz)	S2B	0.00102	26.44	1.431	36	8	33.67	2.73	24	6	127.3	0.013	39.96	2.225	25	7	151.1	<0.0001	36	2.213	21	4	106.9	0.518	90.1	0.217
	8	Accommodation	S2C	0.05611	4.037	0.499	35	8	3.148	0.5805	23	6	78.0	0.319	2.139	0.184	25	7	53.0	0.049	2.341	0.314	21	4	74.4	0.4014	109.4	0.568
	9	AP threshold (mV)	S3A	0.91986	-40.8	0.929	37	8	-42.1	1.143	24	6	103.3	0.359	-41.6	0.717	25	7	102.1	0.5032	-40	0.657	21	4	95.0	0.1294	96.1	0.109
	10	AP amplitude (mV)	S3B	0.91986	85.92	1.289	37	8	86.86	1.213	24	6	101.1	0.617	88.62	1.158	25	7	103.1	0.163	85.98	1.254	21	4	99.0	0.6191	97.0	0.145
	11	AP rise time (ms)	S3C	0.19695	0.578	0.018	37	8	0.567	0.0257	22	6	98.1	0.286	0.568	0.02	25	7	98.3	0.6382	0.535	0.011	21	4	94.4	0.8948	94.3	0.498
	12	AP half-width (ms)	S3D	0.91986	0.848	0.037	37	8	0.853	0.047	24	6	100.6	0.913	0.831	0.047	25	7	98.0	0.4	0.809	0.016	21	4	94.8	0.3604	97.3	0.118
	13	fAHP amplitude (mV)	S3E	0.01071	8.497	0.417	37	8	6.884	0.6674	24	6	81.0	0.035	9.461	0.446	25	7	111.3	0.044	7.71	0.623	21	4	112.0	0.3747	81.5	0.024
	14	sAHP amplitude (mV)	S3F	0.61852	2.276	0.222	37	8	1.951	0.2291	24	6	85.7	0.329	2.191	0.279	25	7	96.3	0.598	1.987	0.217	21	4	101.8	0.6604	90.7	0.861
DGCs Type II	15	Cell capacitance (pF)	1G	6.3E-06	72.03	3.781	21	4	55.4	2.528	32	5	76.9	0.0004	59.08	2.507	22	3	82.0	0.0063	60.86	3.665	22	5	109.9	0.2106	103.0	0.689
	16	Input Resistance (Mohm)	1H	0.00019	276.3	13.29	21	4	318.1	11.76	32	5	115.1	0.0249	342.2	13.57	22	3	123.9	0.0013	344.7	23.01	21	5	108.4	0.3713	100.7	0.764
	17	Firing gain (Hz/pA)	1J	0.23452	0.18	0.014	22	4	0.155	0.0112	32	5	86.2	0.445	0.179	0.012	22	3	99.4	0.9553	0.153	0.01	22	5	98.5	0.6945	85.4	0.097
	18	Rheobase (pA)	1K	0.00192	73.1	4.678	22	4	78.44	5.268	32	5	107.3	0.476	54.72	5.078	22	3	74.9	0.011	64.64	5.788	22	5	82.4	0.089	118.1	0.154
	19	Spike latency (ms)	1L	0.00022	192.9	8.071	22	4	166.2	9.414	32	5	86.2	0.048	148.2	8.063	22	3	76.8	0.0003	167.5	11.21	21	5	100.8	0.9303	113.0	0.166
	20	Resting membrane potential (mV)	S2D	0.12175	-80.3	1.085	22	4	-79.3	0.891	31	5	98.8	0.4878	-83.2	0.983	21	3	103.7	0.0522	-80.7	1.036	21	5	101.7	0.3237	96.9	0.083
	21	Max firing rate (Hz)	S2E	0.00032	43.27	3.803	22	4	37.91	3.068	32	5	87.6	0.275	46.14	3.293	22	3	106.6	0.5722	37.52	3.281	21	5	99.0	0.9345	81.3	0.071
	22	Accommodation	S2F	0.6848	5.178	5.178	22	4	4.807	1.008	32	5	92.8	0.1525	5.353	1.05	22	3	103.4	0.5647	6.05	1.029	21	5	125.9	0.0303	113.0	0.162
	23	AP threshold (mV)	S3G	0.07893	-37.2	0.905	22	4	-38.3	0.7717	32	5	102.9	0.3704	-38.2	0.909	22	3	102.6	0.464	-37.9	-37.9	21	5	99.0	0.7534	99.3	0.848
	24	AP amplitude (mV)	S3H	0.3759	75.36	75.36	22	4	75.18	1.831	32	5	99.8	0.9402	77.89	77.89	22	3	103.4	0.122	75.59	1.431	21	5	100.5	0.8731	97.0	0.218
	25	AP rise time (ms)	S3I	0.00012	0.501	0.008	22	4	0.511	0.5108	32	5	101.9	0.6292	0.498	0.498	22	3	99.4	0.7864	0.526	0.011	21	5	102.9	0.4878	105.5	0.048
	26	AP half-width (ms)	S3J	0.12113	0.722	0.016	22	4	0.726	0.0294	32	5	100.6	0.2166	0.723	0.015	22	3	100.1	0.9684	0.729	0.014	21	5	100.4	0.0701	100.8	0.786
	27	fAHP amplitude (mV)	S3K	0.29974	11.38	0.754	22	4	11.29	11.29	32	5	99.2	0.9329	11.58	0.465	22	3	101.8	0.822	11.27	11.27	21	5	99.8	0.822	97.3	0.731
	28	sAHP amplitude (mV)	S3L	0.44779	1.438	1.438	22	4	1.1	1.1	32	5	76.5	0.2895	1.459	1.459	22	3	101.5	0.5688	1.025	0.103	21	5	93.2	0.5688	70.3	0.018
CA1 PCs	29	Cell capacitance (pF)	S1A	0.00098	150.6	7.489	27	4	161.9	6.216	28	5	107.5	0.2487	131	5.21	30	4	87.0	0.0334	136.7	7.222	21	4	84.4	0.0109	104.4	0.518
	30	Input Resistance (Mohm)	S1B	0.07096	126.9	5.434	24	4	125.7	4.61	24	5	99.1	0.8625	136	4.729	30	4	107.2	0.2082	141.2	6.341	19	4	112.3	0.0487	103.8	0.511
	31	Firing gain (Hz/pA)	S1D	0.01611	0.241	0.01	27	4	0.22	0.0086	30	6	91.3	0.1228	0.249	0.009	30	4	103.6	0.2456	0.238	0.009	21	4	108.5	0.1483	95.6	0.201
	32	Rheobase (pA)	S1E	0.58244	106.4	7.189	27	4	107.7	5.481	30	6	101.2	0.432	102.6	4.848	29	4	96.4	0.9642	102.5	7.104	20	4	95.2	0.4245	99.9	0.689
	33	Spike latency (ms)	S1F	0.48309	250.6	14.9	27	4	257.9	15.28	22	5	102.9	0.736	243.5	9.607	30	4	97.2	0.6836	234.6	14.3	20	4	91.0	0.2739	96.3	0.593
	34	Resting membrane potential (mV)	S2G	0.27683	-67.3	0.776	27	4	-67.2	0.9994	28	5	99.9	0.355	-65.9	0.568	30	4	97.9	0.147	-66	0.982	21	4	98.2	0.16	100.2	0.919
	35	Max firing rate (Hz)	S2H	0.07366	41.04	1.986	27	4	39.33	1.677	30	6	95.8	0.5123	44.63	1.605	30	4	108.7	0.1611	40.95	1.613	21	4	104.1	0.6475	91.8	0.303
	36	Accommodation	S2I	0.7145	2.559	0.198	27	4	3.283	0.463	30	6	128.3	0.2709	2.812	0.222	30	4	109.9	0.4012	3.041	0.236	21	4	92.6	0.5223	108.1	0.495
	37	AP threshold (mV)	S3M	0.76484	-47.2	0.675	27	4	-47.5	0.7298	30	6	100.6	0.7815	-47.1	0.602	30	4	99.7	0.8305	-47.3	0.602	21	4	99.6	0.8647	100.5	0.917
	38	AP amplitude (mV)	S3N	0.11459	88.79	3.248	27	4	94.21	1.269	30	6	106.1	0.0305	91.3	0.965	30	4	102.8	0.9431	93.68	1.711	21	4	99.4	0.5984	102.6	0.02
	39	AP rise time (ms)	S3O	0.58356	0.494	0.008	26	4	0.546	0.0134	30	6	110.6	0.0084	0.508	0.009	30	4	102.8	0.4578	0.531	0.014	21	4	97.2	0.5217	104.6	0.522
	40	AP half-width (ms)	S3P	0.00012	0.787	0.012	27	4	0.875	0.0164	30	6	111.2	<0.0001	0.808	0.013	30	4	102.7	0.1317	0.871	0.021	21	4	99.5	0.857	107.9	0.003
	41	fAHP amplitude (mV)	S3Q	0.02578	7.751	0.37	27	4	7.016	0.4946	30	6	90.5	0.2475	8.832	0.608	30	4	113.9	0.2295	8.418	0.587	21	4	120.0	0.0744	95.3	0.74
	42	sAHP amplitude (mV)	S3R	0.22527	1.229	0.118	27	4	1.797	0.1745	30	6	146.2	0.0107	1.867	0.18	30	4	151.9	0.0054	1.59	0.145	21	4	88.5	0.3965	85.2	0.269
DGCs Type I	43	Cell capacitance (pF)	2D,I		51.35	2.02	11	4	42.62	2.889	24	5	83.0	0.0616	44.3	1.497	12	4	86.3	0.0099	38.79	2.067	37	4	91.0	0.2728	87.6	0.149
	44	Input Resistance (Mohm)	2E,J		446.1	30.27	11	4	472.1	30.27	21	5	105.8	0.5838	509.6	23.27	11	4	114.2	0.0722	507.6	21.25	35	4	107.5	0.1277	99.6	0.959
	45	Firing gain (Hz/pA)	2F,K		0.266	0.024	12	4	0.256	0.0161	24	5	96.2	0.728	0.283	0.021	12	4	106.4	0.6023	0.253	0.017	38	4	98.8	0.9058	89.4	0.368
	46	Rheobase (pA)	2G,L		39.5	3.886	12	4	37.84	2.834	24	5	95.8	0.734	35.5	3.096	12	4	89.9	0.3071	35.32	3.07	38	4	93.3	0.3816	99.5	0.906
	47	Spike latency (ms)	2H,M		141.9	7.754	11	4	126.5	7.397	24	5	89.1	0.216	123.4	5.934	12	4	87.0	0.0696	113	5.609	37	4	89.3	0.1458	91.6	0.326
DGCs Combined	48	Cell capacitance (pF)	2N		64.56	3.026	32	4	50.1	2.039	56	5	77.6	<0.0001	53.86	2.089	34	4	83.4	0.0047	45.76	2.311	59	4	91.3	0.1645	85.0	0.022
	49	Input Resistance (Mohm)	2O		329.7	18.76	32	4	394	20.72	53	5	119.5	0.0389	398.7	18.76	33	4	120.9	0.0113	455.8	20.82	56	4	115.7	0.0376	114.3	0.063
	50	Firing gain (Hz/pA)	2P		0.203	0.012	34	4	0.192	0.0107	56	5	94.9	0.552	0.215	0.014	34	4	106.2	0.4977	0.215	0.013	60	4	111.7	0.1883	99.7	0.979
	51	Rheobase (pA)	2Q		54.42	4.39	34	4	61.04	4.21	56	5	112.2	0.426	41.28	3.792	34	4	75.9	0.0272	46.24	3.364	60	4	75.8	0.0066	112.0	0.355
	52	Spike latency (ms)	2R		175.9	7.271	33	4	149.2	6.736	56	5	84.8	0.012	129.5	5.932	34	4	73.6	0.0002	132.7	6.379	58	4	88.9	0.0784	102.5	0.482

Supplementary Table 2. Detailed information on all neuronal parameters for apoE4-fKI mice presented in Figures 3 and 4

	Parameter	Figure	E4fKI-cre(-) Mean	SEM	n	N	% vs. apoE3	p vs. apoE3	E4fKI-cre(+) Mean	SEM	n	N	% vs. cre-	p vs. cre-	% vs. apoE3	p vs. apoE3
	apoE4-fKI/Syn-cre															
1	CA3 PC Cell capacitance (pF)	3A	151.6	6.382	19	3	73.201	<0.0001	197.1	7.305	19	3	130.0	0.002	95.171	0.9942
2	CA3 PC Input Resistance (Mohm)	3B	326.5	18.29	18	3	157.65	0.0151	258.4	9.618	19	3	79.1	0.0064	99.042	0.8746
3	CA3 PC firing gain (Hz/pA)	3D	0.069	0.005	19	3	145.66	0.0003	0.045	0.005	19	3	65.5	0.0006	95.356	0.9096
4	CA3 PC Rheobase (pA)	3E	120.2	8.082	19	3	74.891	0.0431	182.2	19.27	19	3	151.6	0.0074	113.52	0.2117
5	CA3 PC spike latency (ms)	3F	198.5	12.02	19	3	82.263	0.0632	284	19.65	19	3	143.1	0.0002	117.7	0.0435
	apoE4-fKI/gfap-cre															
6	CA3 PC Cell capacitance (pF)	4A	155.5	5.139	19	3	75.085	<0.0001	147.6	4.425	15	3	94.9	0.7635	71.27	<0.0001
7	CA3 PC Input Resistance (Mohm)	4B	373	16.24	19	3	142.97	0.0001	358.9	24.57	15	3	96.2	0.8568	137.56	0.0021
8	CA3 PC firing gain (Hz/pA)	4D	0.08	0.006	19	3	168.5	0.0002	0.094	0.011	15	3	117.3	0.297	197.73	<0.0001
9	CA3 PC Rheobase (pA)	4E	82.89	12.12	19	3	51.645	<0.0001	81.67	12.53	15	3	98.5	>0.9999	50.885	<0.0001
10	CA3 PC spike latency (ms)	4F	183.7	15.83	19	3	76.129	0.0043	171.3	16.46	15	3	93.2	0.8304	70.99	0.0021

Supplementary Table 3. Detailed information on all synaptic activity recordings in apoE-KI mice presented in Figure 6.

	Parameter	Figure	apoE3-KI										apoE4-KI													
			7-9 months				17-19 months						7-9 months						17-19 months							
			Mean	SEM	n	N	Mean	SEM	n	N	% vs. 7mo	p vs. 7mo	Mean	SEM	n	N	% vs. apoE3	p vs. apoE3	Mean	SEM	n	N	% vs. apoE3	p vs. apoE3	% vs. 7mo	p vs. 7mo
1	CA3 PC sEPSC frequency (Hz)	6A	6.657	1.655	13	5	14.4	3.152	11	4	216.3	0.033	14.99	1.853	19	5	225.2	0.0035	11.12	2.031	10	4	77.2	0.6047	74.2	0.2014
2	CA3 PC sEPSC amplitude (pA)	6B	18.61	2.187	13	5	17.87	2.078	11	4	96.0	>0.9999	19.12	2.276	19	5	102.7	0.9397	13.92	1.615	10	4	77.9	0.1474	72.8	0.1507
3	CA3 PC sIPSC frequency (Hz)	6C	8.216	2.523	7	4	6.482	2.126	16	6	78.9	0.278	10.03	1.69	15	6	122.1	0.5538	6.224	1.042	14	5	96.0	0.918	62.1	0.0702
4	CA3 PC sIPSC amplitude (pA)	6D	17.13	2.155	7	4	16.58	1.776	16	4	96.8	0.859	18.33	2.764	15	6	107.0	0.7843	15.78	1.88	14	5	95.2	0.7599	86.1	0.458
5	CA3 PC E-I Ratio	6E	0.875	0.176	7	4	6.077	2.186	9	4	694.2	0.001	3.631	0.928	12	4	414.8	0.0397	5.139	2.166	9	4	84.6	0.5457	141.5	0.7021
6	DGC sEPSC frequency (Hz)	6F	1.647	0.184	22	6	1.522	0.2113	41	7	92.4	0.178	2.085	0.339	28	6	126.6	0.7826	1.973	0.382	41	10	129.6	0.402	94.6	0.5785
7	DGC sEPSC amplitude (pA)	6G	8.105	0.383	22	6	8.306	0.353	41	7	102.5	0.459	9.169	0.633	28	6	113.1	0.3772	7.766	0.486	41	10	93.5	0.3709	84.7	0.0793
8	DGC sIPSC frequency (Hz)	6H	2.522	0.346	19	6	2.162	0.3359	37	7	85.7	0.12	1.794	0.258	26	6	71.1	0.0544	0.617	0.068	41	10	28.5	0.001	34.4	<0.0001
9	DGC sIPSC amplitude (pA)	6I	8.203	0.397	19	6	10.42	0.6348	37	7	127.0	0.071	9.439	0.678	26	6	115.1	0.3309	9.316	0.619	41	10	89.4	0.2184	98.7	0.897
10	DGC E-I Ratio	6J	1.985	0.549	18	6	1.81	0.6487	30	7	91.2	0.24	2.319	0.348	24	6	116.8	0.1927	4.558	0.968	33	10	251.8	0.0046	196.6	0.475

Supplementary Table 4. Detailed information on all recordings in CRISPRi-transduced (mCherry+) and control (mCherry-) neurons in apoE4-KI mice presented in Figures 8 and S6.

	Parameter	Figure	mCherry -				mCherry +				
			Mean (norm)	SEM (norm)	n	N	Mean (% mCherry-)	SEM (% mCherry-)	n	N	p vs. mCherry-
	Nell2 CRISPRi										
1	CA3 PC Cell capacitance	8B	100	8.052	14	5	137.1	14.77	13	5	0.04
2	CA3 PC Input Resistance	8C	100	5.437	13	5	81.49	3.684	13	5	0.0099
3	CA3 PC firing gain	8E	100	10.77	13	5	66.4	11.31	12	5	0.0423
4	CA3 PC Rheobase	8F	100	5.095	13	5	186.4	18.31	13	5	0.0005
5	CA3 PC spike latency	8G	100	5.805	14	5	127.2	7.951	13	5	0.01
6	DGC Cell capacitance	8K	100	10.78	18	4	164	28.58	19	4	0.0477
7	DGC Input Resistance	8M	100	4.991	19	4	94.13	6.75	18	4	0.3785
8	DGC firing gain	8N	100	9.353	17	4	90.98	6.516	16	4	0.4398
9	DGC Rheobase	8O	100	8.897	19	4	133.3	14.12	16	4	0.0472
10	DGC spike latency	8P	100	6.667	18	4	140.8	14.81	17	4	0.0153
	Mdga2 CRISPRi										
11	DGC Cell capacitance	S6H	100	9.669	16	3	120.1	12.21	19	3	0.3011
12	DGC Input Resistance	S6I	100	6.117	14	3	100.3	7.319	15	3	0.9768
13	DGC firing gain	S6K	100	5.533	16	3	93.5	7.759	17	3	0.5051
14	DGC Rheobase	S6L	100	13.41	14	3	117.6	9.501	13	3	0.302
15	DGC spike latency	S6M	100	6.808	15	3	114.3	6.222	14	3	0.1344